Astronomy & Astrophysics manuscript no. output
May 6, 2026

Euclid preparation

XCIX. Cosmology Likelihood for Observables in Euclid (CLOE). 6: Impact of systematic uncertainties on the cosmological analysis

Euclid Collaboration: L. Blot[⋆1,2], K. Tanidis[3], G. Cañas-Herrera[4,5], P. Carrilho[6,7], M. Bonici[8,9], S. Camera[10,11,12], V. F. Cardone[13,14], S. Casas[15,16], S. Davini[17], S. Di Domizio[18,17], S. Farrens[19], L. W. K. Goh[19], S. Gouyou Beauchamps[20,21], S. Ilić[22,23], S. Joudaki[24], F. Keil[23], A. M. C. Le Brun[2], M. Martinelli[13,14], C. Moretti[25,26,27,28], V. Pettorino[4], A. Pezzotta[29], Z. Sakr[30,23,31], A. G. Sánchez[32], D. Sciotti[13,14], I. Tutusaus[21,20,23], V. Ajani[19,33,34], M. Crocce[21,20], A. Fumagalli[25], C. Giocoli[35,36], L. Legrand[37,38], M. Lembo[39,40,41], G. F. Lesci[42,35], D. Navarro-Gironés[5], A. Nouri-Zonoz[43], S. Pamuk[44], A. Pourtsidou[7,45], M. Tsedrik[7,45], J. Bel[46], C. Carbone[9], C. A. J. Duncan[7], M. Kilbinger[19], D. Sapone[47], E. Sellentin[48,5], P. L. Taylor[49,50], L. Amendola[30], S. Andreon[29], N. Auricchio[35], C. Baccigalupi[26,25,27,28], M. Baldi[51,35,36], S. Bardelli[35], P. Battaglia[35], A. Biviano[25,26], E. Branchini[18,17,29], M. Brescia[52,53], V. Capobianco[12], J. Carretero[24,54], M. Castellano[13], G. Castignani[35], S. Cavuoti[53,55], K. C. Chambers[56], A. Cimatti[57], C. Colodro-Conde[58], G. Congedo[7], C. J. Conselice[59], L. Conversi[60,61], Y. Copin[62], F. Courbin[63,64,65], H. M. Courtois[66], M. Cropper[67], A. Da Silva[68,69], H. Degaudenzi[70], S. de la Torre[71], G. De Lucia[25], H. Dole[72], M. Douspis[72], F. Dubath[70], X. Dupac[61], S. Dusini[73], S. Escoffier[74], M. Farina[75], F. Faustini[13,76], S. Ferriol[62], F. Finelli[35,77], M. Frailis[25], E. Franceschi[35], M. Fumana[9], S. Galeotta[25], K. George[78], W. Gillard[74], B. Gillis[7], J. Gracia-Carpio[32], A. Grazian[79], F. Grupp[32,80], S. V. H. Haugan[81], H. Hoekstra[5], W. Holmes[82], I. M. Hook[83], F. Hormuth[84], A. Hornstrup[85,86], K. Jahnke[87], M. Jhabvala[88], B. Joachimi[89], E. Keihänen[90], S. Kermiche[74], B. Kubik[62], M. Kümmel[80], M. Kunz[43], H. Kurki-Suonio[91,92], O. Lahav[89], S. Ligori[12], P. B. Lilje[81], V. Lindholm[91,92], I. Lloro[93], G. Mainetti[94], D. Maino[95,9,96], E. Maiorano[35], O. Mansutti[25], O. Marggraf[97], K. Markovic[82], N. Martinet[71], F. Marulli[42,35,36], R. J. Massey[98], E. Medinaceli[35], S. Mei[99,100], Y. Mellier[101,39], M. Meneghetti[35,36], E. Merlin[13], G. Meylan[102], A. Mora[103], L. Moscardini[42,35,36], E. Munari[25,26], R. Nakajima[97], C. Neissner[104,54], S.-M. Niemi[4], C. Padilla[104], S. Paltani[70], F. Pasian[25], K. Pedersen[105], W. J. Percival[8,106,107], S. Pires[19], G. Polenta[76], M. Poncet[108], L. A. Popa[109], L. Pozzetti[35], F. Raison[32], A. Renzi[110,73], J. Rhodes[82], G. Riccio[53], E. Romelli[25], M. Roncarelli[35], C. Rosset[99], R. Saglia[80,32], B. Sartoris[80,25], P. Schneider[97], T. Schrabback[111], A. Secroun[74], E. Sefusatti[25,26,27], G. Seidel[87], S. Serrano[20,112,21], P. Simon[97], C. Sirignano[110,73], G. Sirri[36], A. Spurio Mancini[113], L. Stanco[73], J.-L. Starck[19], J. Steinwagner[32], C. Surace[71], P. Tallada-Crespí[24,54], A. N. Taylor[7], I. Tereno[68,114], N. Tessore[67], S. Toft[115,116], R. Toledo-Moreo[117], F. Torradeflot[54,24], E. A. Valentijn[118], L. Valenziano[35,77], J. Valiviita[91,92], T. Vassallo[25,78], A. Veropalumbo[29,17,18], Y. Wang[119], J. Weller[80,32], A. Zacchei[25,26], G. Zamorani[35], F. M. Zerbi[29], E. Zucca[35], M. Ballardini[40,41,35], M. Bolzonella[35], A. Boucaud[99], E. Bozzo[70], C. Burigana[120,77], R. Cabanac[23], M. Calabrese[121,9], A. Cappi[122,35], J. A. Escartin Vigo[32], L. Gabarra[3], J. García-Bellido[123], W. G. Hartley[70], R. Maoli[124,13], J. Martín-Fleitas[125], M. Maturi[30,126], N. Mauri[57,36], R. B. Metcalf[42,35], M. Pöntinen[91], I. Risso[29,17], V. Scottez[101,127], M. Sereno[35,36], M. Tenti[36], M. Viel[26,25,28,27,128], M. Wiesmann[81], Y. Akrami[123,129], S. Alvi[40], I. T. Andika[130,131], S. Anselmi[73,110,132], M. Archidiacono[95,96], F. Atrio-Barandela[133], E. Aubourg[99,134], L. Bazzanini[40,35], M. Bethermin[135], A. Blanchard[23], S. Borgani[136,26,25,27,128], M. L. Brown[59], S. Bruton[137], A. Calabro[13], F. Caro[13], C. S. Carvalho[114], T. Castro[25,27,26,128], F. Cogato[42,35], S. Conseil[62], O. Cucciati[35], G. Desprez[118], A. Díaz-Sánchez[138], J. M. Diego[44], M. Y. Elkhashab[25,27,136,26], Y. Fang[80], A. G. Ferrari[36], P. G. Ferreira[3], A. Finoguenov[91], A. Franco[139,140,141], K. Ganga[99], T. Gasparetto[13], V. Gautard[142], R. Gavazzi[71,39], E. Gaztanaga[21,20,143], F. Giacomini[36], F. Gianotti[35], G. Gozaliasl[144,91], A. Gruppuso[35,36], M. Guidi[51,35], C. M. Gutierrez[145], H. Hildebrandt[146], J. Hjorth[105], J. J. E. Kajava[147,148], Y. Kang[70], V. Kansal[149,150], D. Karagiannis[40,151], K. Kiiveri[90], J. Kim[3], C. C. Kirkpatrick[90], S. Kruk[61], M. Lattanzi[41], V. Le Brun[71], F. Lepori[152], G. Leroy[153,98], J. Lesgourgues[15], L. Leuzzi[35], T. I. Liaudat[134], J. Macias-Perez[154], M. Magliocchetti[75], F. Mannucci[155], C. J. A. P. Martins[156,157], L. Maurin[72], M. Migliaccio[158,159], M. Miluzio[61,160], P. Monaco[136,25,27,26], A. Montoro[21,20], G. Morgante[35], S. Nadathur[143], K. Naidoo[143,89], A. Navarro-Alsina[97], S. Nesseris[123], L. Pagano[40,41], D. Paoletti[35,77], F. Passalacqua[110,73], K. Paterson[87], R. Paviot[19], A. Pisani[74], D. Potter[152], S. Quai[42,35], M. Radovich[79], W. Roster[32], S. Sacquegna[161], M. Sahlén[162], D. B. Sanders[56], E. Sarpa[28,128,27], J. Schaye[5], A. Schneider[152], L. C. Smith[163],

Article published by EDP Sciences, to be cited as https://doi.org/10.1051/0004-6361/202557700

J. G. Sorce[164,72], J. Stadel[152], C. Tao[74], G. Testera[17], R. Teyssier[165], S. Tosi[18,17,29], A. Troja[110,73], M. Tucci[70], A. Venhola[166], D. Vergani[35], F. Vernizzi[167], G. Verza[168,169], S. Vinciguerra[71], and N. A. Walton[163]

(Affiliations can be found after the references)

May 6, 2026

ABSTRACT

Extracting cosmological information from the *Euclid* galaxy survey will require modelling numerous systematic effects during the inference process. This implies varying a large number of nuisance parameters, which have to be marginalised over before reporting the constraints on the cosmological parameters. This is a delicate process, especially with such a large parameter space, which could result in biased cosmological results. In this work, we study the impact of different choices for modelling systematic effects and prior distribution of nuisance parameters for the final *Euclid* Data Release, focusing on the 3×2pt analysis for photometric probes and the galaxy power spectrum multipoles for the spectroscopic probes. We explore the effect of intrinsic alignments, linear galaxy bias, magnification bias, multiplicative cosmic shear bias, and shifts in the redshift distribution for the photometric probes, as well as the purity of the spectroscopic sample. We find that intrinsic alignment modelling has the most severe impact with a bias up to $6\,\sigma$ on the Hubble constant H_0 if neglected, followed by mis-modelling of the redshift evolution of galaxy bias, yielding up to $1.5\,\sigma$ on the parameter $S_8 \equiv \sigma_8 \sqrt{\Omega_m/0.3}$. Choosing a too optimistic prior for multiplicative bias can also result in biases of the order of $0.7\,\sigma$ on S_8. We also find that the precision on the estimate of the purity of the spectroscopic sample will be an important driver for the constraining power of the galaxy clustering full-shape analysis. These results will help prioritise efforts to improve the modelling and calibration of systematic effects in *Euclid*.

Key words. galaxy clustering–weak lensing–*Euclid* survey– systematic effects

1. Introduction

Large-scale galaxy surveys are now providing us with very competitive constraints on cosmological models. Observational programmes such as the spectroscopic redshift surveys Sloan Digital Sky Survey (SDSS, Alam et al. 2015) and the Dark Energy Spectroscopic Instrument (DESI, Novell-Masot et al. 2025), and the photometric surveys Dark Energy Survey (DES, DES Collaboration: Abbott et al. 2025), Kilo Degree Survey (KiDS, Wright et al. 2025), and Hyper Supreme Cam (HSC, Dalal et al. 2023), have significantly improved our understanding of the large-scale structure of the Universe. Experiments that have recently commenced data collection, such as the *Euclid* space telescope (Euclid Collaboration: Mellier et al. 2025) and the Vera C. Rubin Observatorys Legacy Survey of Space and Time (LSST, LSST Science Collaboration: Abell et al. 2009; LSST Dark Energy Science Collaboration: Mandelbaum et al. 2018; Ivezić et al. 2019) are expected to push these constraints even further. The *Euclid* mission stands out as a particularly powerful probe of fundamental physics by combining photometric and spectroscopic probes to provide extremely tight constraints on the time evolution of dark energy and deviations from general relativity at large scales.

It has become increasingly clear that one of the primary challenges in the cosmological analysis of such probes is the size of the parameter space to be explored. Although the concordance ΛCDM model only relies on six cosmological parameters, exploring extensions to this model requires larger parameter spaces, often with some of the extra parameters being poorly constrained (see e.g., Ivanov et al. 2020; Garcia-Quintero et al. 2020). Moreover, each observable is affected by a different set of systematic effects that need to be taken into account. Instrumental calibration, photometric redshift uncertainties, as well as modelling uncertainties in galaxy clustering and weak lensing all introduce biases that must be carefully mitigated to extract unbiased cosmological information (Euclid Collaboration: Paykari et al. 2020; Cragg et al. 2022; Euclid Collaboration: Lepori et al. 2022; Euclid Collaboration: Tanidis et al. 2024; LSST Dark Energy Science Collaboration: Awan et al. 2025).

Previous analyses have devoted significant effort to identifying many systematic effects that are present in large-scale galaxy surveys and understanding how to mitigate their impact (Liu et al. 2016; Berlfein et al. 2024). In many cases, this is done by modelling the systematic effect with a parametric model and treating its parameters as nuisance parameters, which will be marginalised before presenting the constraints on the cosmological parameters (Myles et al. 2021). The main problem of allowing these nuisance parameters to vary and absorb the residual systematic effects is that part of the constraining power will be devoted to constraining these parameters, which generally do not contain relevant cosmological information.

One option to compensate for the loss of constraining power is to add informative priors on the nuisance parameters. This is only possible when the choice of the prior can be motivated by our previous knowledge of the performance of the instrument or the physics that generates the systematic uncertainty (see again Myles et al. 2021). In fact, using ill-motivated priors that might be too tight or incorrectly located might end up biasing the main cosmological parameter constraints and result in false detections of physics beyond the standard cosmological model (Sun et al. 2009).

Because of all this, it is very important to understand at which level systematic effects can impact the cosmological results and how sensitive our baseline results are to different choices of modelling and priors on the systematic uncertainties. In this article, we explicitly address this point by answering the following questions.

1. Whether we can fix some of the nuisance parameters to reduce the size of the parameter space without incurring biases on the cosmological parameters.
2. Whether our modelling of systematics is too complex, resulting in poorly constrained nuisance parameters.
3. Whether our modelling of systematics is too simplistic or incorrect, resulting in biases on the cosmological parameters.
4. Whether our prior is too conservative, resulting in loss of constraining power.
5. Whether our prior is too optimistic, resulting in biases on the cosmological parameters.

⋆ e-mail: linda.blot@ipmu.jp

The answers to these questions will guide us in how to define an optimal analysis set-up that maximises the cosmological information while ensuring unbiased constraints from *Euclid* data. We based our work on the survey specifications for the final *Euclid* Data Release and used `CLOE`, the official *Euclid* likelihood code, which is presented in Euclid Collaboration: Cardone et al. (2025), Euclid Collaboration: Joudaki et al. (2026), Euclid Collaboration: Cañas-Herrera et al. (2025), and Euclid Collaboration: Martinelli et al. (2025).

The paper is organised as follows. In Sect. 2, we present the main systematic effects that are present in *Euclid* photometric observables. The systematic effects that are important for the spectroscopic observables are described in Sect. 3. We then present the list of priors and baselines considered in this analysis in Sect. 4 and the main results of our analysis in Sect. 5. Finally, we summarise our findings and present our conclusions in Sect. 6.

2. Photometric observables and their systematic effects

The imaging survey of *Euclid* will provide the 2D positions, photometric redshifts and shapes of almost 1.5 billion galaxies. Based on these measurements, we will be able to construct the 3×2pt summary statistics of the so-called photometric galaxy clustering (GCph), the weak lensing (WL), and the galaxy-galaxy lensing (XC) observable, which is the cross-correlation between galaxy clustering and weak lensing. We will only report here the relevant definitions and refer the reader to Euclid Collaboration: Cardone et al. (2025) for the full description of the observables and their theoretical modelling.

In this study, we focus on the angular power spectra, which we denote as $C_{ij}^{AB}(\ell)$ at the angular multipole, ℓ, for observable, A, in redshift bin i and observable B in redshift bin j. These can be expressed as integrals of the 3D power spectra, $P_{AB}^{\rm photo}(k,z)$, at wavevector k and redshift z as

$$C_{ij}^{AB}(\ell) = \int_0^{z_{\rm max}} {\rm d}z \, \frac{c\, W_i^A(\ell,z)\, W_j^B(\ell,z)}{H(z)\, f_K^2[r(z)]} P_{AB}^{\rm photo}\left[\frac{\ell+1/2}{f_K[r(z)]}, z\right] , \quad (1)$$

where $W_i^A(\ell,z)$ is the ℓ- and z-dependent kernel, $H(z)$ is the Hubble function, $f_K[r(z)]$ is the comoving distance for a curvature value K, and $z_{\rm max}$ the maximum redshift of the survey. We used the Limber approximation (Kaiser 1992), which is valid for $\ell \gg 1$ and accurate in the case of broad redshift bins (as are the photometric estimates). Under this limit, we relate the wavevector, k, to the multipole, ℓ, as

$$k = \frac{\ell+1/2}{f_K[r(z)]} . \quad (2)$$

In this work, we used the `HMcode` (Mead et al. 2021) non-linear emulator described in Euclid Collaboration: Carrilho et al. in prep. for the 3D power spectra, $P_{AB}^{\rm photo}(k,z)$.

2.1. Weak lensing

It is well known that the intervening matter deflects the paths of photons emitted by distant sources, resulting in the distortion of their images. This distortion can be decomposed into the spin-0 convergence field, κ, and the spin-2 shear field, γ. These describe the size magnification (circles) and the distortion of the galaxy shape (ellipses) in different directions, respectively. Both contain useful cosmological information, but the convergence is harder to model due to the necessity of prior knowledge about the true size of the source (Heavens et al. 2013; Alsing et al. 2015) and is also more prone to bias (Hoekstra et al. 2017). Therefore, the common WL observable in large-scale-structure surveys is cosmic shear.

The correlation of galaxy shapes across different scales thus carries information about the distribution of matter along the line of sight. However, cosmological information is contaminated by the intrinsic correlation of shapes due to local interactions between source galaxies, an effect called intrinsic alignments (hereafter IA, Joachimi et al. 2015). The WL power spectra will then be a combination of shear and IA correlations, which can be expressed as

$$C_{ij}^{\rm WL}(\ell) = C_{ij}^{\gamma\gamma}(\ell) + C_{ij}^{\rm II}(\ell) + C_{ij}^{\gamma{\rm I}}(\ell) , \quad (3)$$

where $C_{ij}^{\gamma\gamma}(\ell)$ is the shear power spectrum, $C_{ij}^{\gamma{\rm I}}(\ell)$ is the cross-power spectrum between shear and IA, and $C_{ij}^{\rm II}(\ell)$ is the IA power spectrum.

The weak lensing observables are also subject to biases due to instrumental effects (Cropper et al. 2013) and systematic errors due to mis-determination of the redshift distribution of the sources and lenses (Euclid Collaboration: Desprez et al. 2020; Naidoo et al. 2023). These effects are expected to be kept under control thanks to the data calibration process, and therefore it is considered safe to use Gaussian priors for the nuisance parameters related to them (Cropper et al. 2016; Euclid Collaboration: Martinet et al. 2019; Euclid Collaboration: Schirmer et al. 2022; Jansen et al. 2024; Euclid Collaboration: Cropper et al. 2025; Euclid Collaboration: Congedo et al. 2024; Euclid Collaboration: McCracken et al. 2025).

2.1.1. Intrinsic alignments

The IA of galaxy shapes, as we introduced in Sect. 2.1, is caused by tidal gravitational fields in large-scale structures that align nearby galaxies, as well as events such as galaxy mergers, which influence the relative alignments of both shapes and angular momenta throughout their evolution. To model this signal, we computed $C_{ij}^{\rm II}(\ell)$ and $C_{ij}^{\gamma{\rm I}}(\ell)$ as in Eqs. (33–35) of Euclid Collaboration: Cardone et al. (2025). These involve the $P_{\rm II}$ and $P_{\rm Im}$ power spectra respectively, which we relate to the matter power spectrum, $P_{\rm mm}$, as

$$P_{\rm II}(k,z) = [f_{\rm IA}(z)]^2\, P_{\rm mm}(k,z) , \quad (4)$$

$$P_{\rm Im}(k,z) = f_{\rm IA}(z)\, P_{\rm mm}(k,z) . \quad (5)$$

The IA prefactor is defined as

$$f_{\rm IA}(z) = -\mathcal{A}_{\rm IA}\, C_{\rm IA} \rho_{\rm crit,0}\, \frac{\Omega_{\rm m,0}}{D(z)} \left(\frac{1+z}{1+z_0}\right)^{\eta_{\rm IA}} , \quad (6)$$

with $\Omega_{\rm m,0}$ the matter fraction today, $D(z)$ the linear growth factor, and z_0 the pivot redshift (arbitrarily set to zero here). This is called the redshift-dependent non-linear alignment (zNLA) model (Joachimi et al. 2011). The nuisance parameters of the model are the dimensionless amplitude $\mathcal{A}_{\rm IA}$ and redshift exponent $\eta_{\rm IA}$. We fix the conventional normalisation constant to $C_{\rm IA} = 5 \times 10^{-14}\, h^{-2} M_\odot^{-1} {\rm Mpc}^3$, which enters through the dimensionless combination $C_{\rm IA}\rho_{\rm crit,0}$. Since $C_{\rm IA}$ is fully degenerate with $\mathcal{A}_{\rm IA}$, it is kept fixed following Euclid Collaboration: Mellier et al. (2025). While there are more sophisticated IA models in the literature (e.g. TATT, Blazek et al. 2015), as we show in the following, we can already see significant effects due to mismodelling even within this simpler model.

2.1.2. Shear bias

Additional contamination of the shear field can come from instrumental effects such as point spread function (PSF) modelling errors, selection effects, blending, or measurement errors of the galaxy shape (Huterer et al. 2006; Massey et al. 2013; Mandelbaum 2018). These contributions can be multiplicative or additive to the shear signal (Massey et al. 2013). For example, PSF size modelling errors and pixel noise cause a multiplicative effect (Melchior & Viola 2012; Refregier et al. 2012; Bernstein 2010), while the anisotropy of the modelled PSF, induced by elliptical PSFs or unaccounted for charge transfer inefficiencies, can cause an additive effect. The former can be determined using image simulations (Hoekstra et al. 2017; Kannawadi et al. 2019; Pujol et al. 2020) and the latter can be inferred from the data itself using empirical null tests (van Uitert & Schneider 2016; Li et al. 2023). Furthermore, both of these effects can be redshift- or scale-dependent. For instance, colour-dependent PSF errors related to an incorrect modelling of the spectral energy distributions (SEDs) of galaxies induce redshift-dependent shear biases (Semboloni et al. 2013; Eriksen & Hoekstra 2018; Schutt et al. 2025), and the thermal variations due to the solar aspect angle of the spacecraft as it observes in orbit induce spatially varying contributions (Cragg et al. 2022). Once determined, the shear biases are subtracted from the data. However, we expect some residuals to remain, especially from the redshift-dependent multiplicative bias. Accounting for these residuals amounts to transforming the WL power spectra with a multiplicative factor that depends on the parameter m_i for each redshift bin, i, as

$$C_{ij}^{\rm WL}(\ell) \longrightarrow (1+m_i)\,(1+m_j)\,C_{ij}^{\rm WL}(\ell)\ . \tag{7}$$

Although in principle multiplicative bias can be scale dependent, Kitching et al. (2019) showed that it is sufficient to consider a mean factor, m, provided that the spatial variations are small.

2.1.3. Redshift shifts in WL

In order to account for biases in the calibration of the photometric redshift distribution, we allowed for a shift, Δz_i, in the mean of the redshift distribution of the sources, $n_i^{\rm S}(z)$, in each bin, i, following Abbott et al. (2016), such that

$$n_i^{\rm S}(z) \longrightarrow n_i^{\rm S}\,(z-\Delta z_i)\ . \tag{8}$$

The reference values of the Δ_z parameters were derived from the Flagship 2.1 simulation (Euclid Collaboration: Castander et al. 2025).

2.2. Photometric galaxy clustering

We measured photometric galaxy clustering (GCph) by correlating the 2D positions of galaxies on the sky in tomographic redshift bins and measuring their angular power spectrum $C_{\rm GG}(\ell)$. This receives contributions from the clustering of galaxies within the sample and from galaxies that scatter in and out of the sample due to lensing magnification, which modify both their size and luminosity. Therefore, the galaxy clustering angular power spectra take the form

$$C_{ij}^{\rm GG}(\ell) = C_{ij}^{\rm gg}(\ell) + C_{ij}^{\mu\mu}(\ell) + C_{ij}^{\rm g\mu}(\ell)\ , \tag{9}$$

where the first term is the galaxy-galaxy, the second the magnification-magnification, and the third the galaxy-magnification contribution.

2.2.1. Galaxy bias

Galaxies are biased tracers of the matter density field (Kaiser 1987). The bias can in principle be a function of both redshift and scale, but in this work we consider a linear scale-independent bias (Abbott et al. 2018). The galaxy-galaxy power spectrum then reads

$$P_{\rm gg}^{\rm photo}\left[\frac{\ell+1/2}{f_K[r(z)]},\,z\right] = b^2(z)\,P_{\rm mm}^{\rm photo}\left[\frac{\ell+1/2}{f_K[r(z)]},\,z\right]\ , \tag{10}$$

where $b(z)$ the redshift-dependent galaxy bias. To model the redshift dependence, we measured the linear bias in each of the photometric redshift bins in the Flagship 2.1 simulation (Euclid Collaboration: Castander et al. 2025). We then fitted a polynomial function,

$$b(z) = \sum_{i=0}^{3} b_{{\rm gph},i}\,z^i\ , \tag{11}$$

and used the $b_{{\rm gph},i}$ parameters to build our reference data vector. In the following, we also explore the case in which the bias is modelled as a constant within each tomographic redshift bin, i, where the reference values are those obtained from the Flagship 2.1 simulation (Euclid Collaboration: Castander et al. 2025).

2.2.2. Linear redshift-space distortion (RSD)

The linear RSD signal results in the squashing of the galaxy power spectrum at large scales in the direction perpendicular to the line of sight due to the coherent motion of galaxies towards large and highly dense regions (Kaiser 1987). In harmonic space and in the Limber approximation, it takes the form described by the Eqs. (45–47) of Euclid Collaboration: Cardone et al. (2025). We note that in this formalism we did not introduce extra parameters to marginalise over, but rather a fixed correcting term per redshift bin to add in the kernel for galaxy clustering. The physical meaning of these terms is that, effectively, at large scales, galaxies are shuffled among neighbouring redshift bins (Tanidis & Camera 2019). Since the significance of the linear RSD in the photometric observables for *Euclid* to avoid biases (up to $\sim 5\,\sigma$) on the cosmological parameters has been studied thoroughly in Euclid Collaboration: Tanidis et al. (2024), we did not test their impact here. However, we always included them in the computation of the data and the theory vectors.

2.2.3. Magnification bias

The second and third terms of Eq. (9) are shown in Eqs. (42) and (43) of Euclid Collaboration: Cardone et al. (2025). The magnification kernel $W_i^{\mu}(z)$ includes the function $b_{\rm mag}(z)$, which is the magnification bias (Schmidt et al. 2009a,b). This is a lensing contribution in the galaxy clustering of the lenses sample related to the size magnification of the galaxies. It is defined as $b_{\rm mag}(z) = 5\,s(z) - 2$, where $s(z)$ is the logarithmic slope of the luminosity function for the lenses (Scranton et al. 2005; Ménard et al. 2010; Hildebrandt et al. 2009). The magnification effect is two-fold. On the one hand, it means that the distribution of the objects in the images is over larger angles, reducing their number density; on the other hand, the same effect allows for the observation of fainter objects. The impact of ignoring the magnification bias in galaxy surveys has been shown in Duncan et al. (2013) and Tanidis et al. (2019). The effect of neglecting it in the *Euclid* photometric observables has been studied in Euclid Collaboration: Lepori et al. (2022), where they measured biases of up to

$\sim 6\,\sigma$ on the cosmological parameters. Similarly to the galaxy bias, we considered two models for the magnification bias. The first was to account for the magnification bias with one parameter per tomographic redshift bin (evaluated at the centre of the bin), and the second was a polynomial function of redshift,

$$b_{\rm mag}(z) = \sum_{i=0}^{3} b_{{\rm mag},i}\, z^i \,, \tag{12}$$

which is expected to be a good approximation given that the redshift evolution of the magnification bias is smooth. We defined our reference values for the magnification bias parameters using the measurements from the Flagship 2.1 simulation (Euclid Collaboration: Castander et al. 2025).

2.2.4. Redshift shifts in GC

As we did for the source sample, we also accounted for biases in the photometric redshift distribution of the lens sample $n_i^{\rm L}(z)$ as

$$n_i^{\rm L'}(z) = n_i^{\rm L}\,(z - \Delta z_i) \,. \tag{13}$$

The reference values of the Δ_z parameters were derived from the Flagship 2.1 simulation (Euclid Collaboration: Castander et al. 2025).

2.3. Galaxy-galaxy lensing

It has been shown (e.g. Joudaki & Kaplinghat 2012; Tutusaus et al. 2020) that the cross-correlation spectra between the weak lensing and the galaxy clustering observables (also called galaxy-galaxy lensing) significantly improve the constraining power on the cosmological parameters. Therefore, we also included them in this analysis and defined them as

$$C_{ij}^{\rm GL}(\ell) = C_{ij}^{\rm g\gamma}(\ell) + C_{ij}^{\rm gI}(\ell) + C_{ij}^{\mu\gamma}(\ell) + C_{ij}^{\mu\rm I}(\ell) \,, \tag{14}$$

with the individual terms described in Eqs. (55–57) of Euclid Collaboration: Cardone et al. (2025). The terms on the right-hand side of Eq. (14) represent the cross-correlation between galaxy positions and cosmic shear, galaxy positions and intrinsic alignment, magnification and cosmic shear, and magnification and intrinsic alignment, respectively. These terms do not introduce any additional systematic effects.

3. Spectroscopic observables and their systematic effects

The spectroscopic survey of *Euclid* will target emission-line galaxies and measure their redshift using the Hα emission line for around 30 million galaxies, making it possible to map their 3D distribution (Euclid Collaboration: Mellier et al. 2025). The main cosmological probe will be the anisotropic galaxy power spectrum expanded in Legendre multipoles $P_\ell(k; z)$, as defined in Eq. (90) of Euclid Collaboration: Cardone et al. (2025). We used the non-linear model described in Euclid Collaboration: Crocce et al. in prep., which is based on the Effective-Field Theory of Large-Scale Structure (EFTofLSS, see e.g. Euclid Collaboration: Moretti et al. in prep. and references therein). This model comes with a series of nuisance parameters that are known to cause issues such as prior-volume and projection effects (Simon et al. 2023; Carrilho et al. 2023; Maus et al. 2023; Donald-McCann et al. 2023; Zhao et al. 2024; Holm et al. 2023; Morawetz et al. 2025). The strategy to mitigate such effects has been investigated in Euclid Collaboration: Pezzotta et al. in prep. and is therefore beyond the scope of this work.

3.1. Redshift errors

The uncertainty in the spectroscopic redshift estimation causes a smearing of the distribution of galaxies along the line of sight, which must be taken into account in the model. This is done by multiplying the model for the power spectrum by a factor of

$$F_z(k, \mu_k, z) = {\rm e}^{-k^2 \mu_k^2 \sigma_r^2(z)} \,, \tag{15}$$

where μ_k is the cosine of the angle between $\boldsymbol{k}$ and the line of sight, and $\sigma_r(z)$ is the error in the estimation of the comoving distance, which is related to the redshift error, σ_z, through

$$\sigma_r(z) = \frac{c\,\sigma_z}{H(z)} \,. \tag{16}$$

In this work, we fixed $\sigma_z = 0.002$, which is a conservative estimate of the expected precision of the spectroscopic redshift estimation (Euclid Collaboration: Grannet et al. in prep.).

3.2. Purity and completeness

The sample of Hα galaxies can be contaminated by galaxies whose redshift is misestimated due to line misidentification (line interlopers) or random redshift errors (noise interlopers). These galaxies will impact the clustering signal in distinct ways: line interlopers will have their own clustering signal that will be mixed up with the clustering of Hα galaxies, while noise interlopers will lead to a fraction of galaxies in the sample being random outliers that do not cluster. Both of these effects result in a damping of the clustering signal, with an additional deterministic scale-dependence in the case of line interlopers alone.

The number density of measured objects can thus be related to the correct one as

$$n_{\rm meas}(z) = n_{\rm corr}(z)\,\frac{1 - f_{\rm inc}}{1 - f_{\rm out}} \,, \tag{17}$$

where $f_{\rm inc} = 1 - f_{\rm comp}$ is the fraction of undetected Hα galaxies, $f_{\rm comp}$ is the fraction of correctly identified Hα galaxies with respect to the total Hα population (completeness), $f_{\rm out} = 1 - f_{\rm pur}$ is the fraction of outliers, and $f_{\rm pur}$ is the fraction of actual Hα galaxies in the sample (purity).

In this work, we only modelled the effect of noise interlopers on the galaxy power spectrum and left the modelling of line interlopers to future work. Preliminary works, such as Euclid Collaboration: Risso et al. (2026) and Euclid Collaboration: Lee et al. in prep., showed that ignoring the effect of line interlopers does not bias the cosmological parameter constraints, so we do not expect this choice to have a significant impact on the results presented here. The measured galaxy power spectrum multipoles will then become

$$P_{\ell,{\rm meas}}(k; z) = (1 - f_{\rm out})^2\, P_{\ell,{\rm corr}}(k; z) \,. \tag{18}$$

We considered $f_{\rm out}$ as a nuisance parameter and modelled it as a constant within each redshift bin. Our reference values are motivated by end-to-end simulations that include interlopers (Euclid Collaboration: Grannet et al. in prep.), and match the ones used in Euclid Collaboration: Mellier et al. (2025) and Euclid Collaboration: Cañas-Herrera et al. (2025).

4. Method

The aim of this work is to quantify the impact of different modelling and prior choices on the best-fit values and parameter errors, with a focus on cosmological parameters. We started by

defining a synthetic data vector and a set of modelling choices, which were then used to compute the likelihood with `CLOE`. Given a choice for the prior on the parameters, we then sampled the posterior distribution using the `Nautilus` nested sampling algorithm (Lange 2023). Following the same approach as Euclid Collaboration: Cañas-Herrera et al. (2025), we generated noiseless synthetic data vectors with `CLOE` itself, ensuring that any parameter shifts or changes in the constraining power that we observe in our results only arise from the analysis choices that we are testing. For all the tests performed here, we only change the data or the theory vectors and use the data covariance of the baseline set-up. A detailed description of the computation of covariances can be found in Section 5 of Euclid Collaboration: Cañas-Herrera et al. (2025). Since these are analytical covariances, we assume that the likelihood is Gaussian.

Our baseline set-up is the same as the one described in Euclid Collaboration: Cañas-Herrera et al. (2025), which forecasts the expected performance and sample sizes of the final *Euclid* Data Release, with the only exception that in our work we do not assume a Big Bang Nucleosynthesis Gaussian prior on the baryon density parameter $\Omega_{\rm b}h^2$ (Cooke et al. 2018; Schöneberg et al. 2022; Schöneberg 2024). For the photometric observables, we assume a magnitude-limited sample of galaxies with $I_{\rm E} \leq 24.5$ distributed in 13 equi-populated photometric redshift bins between redshift 0.2 and 2.5 (Euclid Collaboration: Mellier et al. 2025). The number density of galaxies was derived using the Flagship 2.1 simulation (Euclid Collaboration: Castander et al. 2025). In our analysis, we consider the high scale cut scenario, where $\ell_{\rm min}({\rm WL}) = \ell_{\rm min}({\rm XC}) = \ell_{\rm min}({\rm GCph}) = 10$ and $\ell_{\rm max}({\rm WL}) = 5000$, while $\ell_{\rm max}({\rm GCph}) = \ell_{\rm max}({\rm XC}) = 3000$. For the spectroscopic observables, we consider a flux-limited sample of Hα galaxies with $f_{\rm H\alpha} > 2 \times 10^{-16}$ erg cm^{-2} s^{-1} in four redshift bins between redshifts 0.9 and 1.8, centred at $\bar{z} \in \{1.0, 1.2, 1.4, 1.65\}$. In this work we analyse the photometric and spectroscopic observables separately. Depending on the analysis choices, the size of the parameter space varies between 16 and 51 dimensions.

In Table 1, we list the reference values and priors of the nuisance parameters that we study in this work, in the baseline set-up. On top of these parameters, we also marginalise over the baryonic feedback efficiency parameter of the `HMcode` emulator $\log_{10}(T_{\rm AGN}/{\rm K})$, which is centred at 7.75 with a Gaussian width of 0.17825. We do not show the impact of modifying this parameter or its degeneracy with the rest of the nuisance parameters, as this has already been investigated in Euclid Collaboration: Carrilho et al. in prep.

When assessing the shifts in a parameter θ with respect to the baseline model, we computed the following quantity:

$$\Delta\sigma_\theta = \frac{\left|\bar{\theta}_{\rm base} - \bar{\theta}\right|}{\sqrt{\sigma^2_{\theta,{\rm base}} + \sigma^2_\theta}}\,, \tag{19}$$

where $\bar{\theta}_{\rm base}$ and $\bar{\theta}$ are the mean values of the parameter posterior in the baseline model and in the model we want to examine, while $\sigma_{\theta,{\rm base}}$ and σ_θ are their corresponding $1\,\sigma$ uncertainties. Equation (19) is equivalent to the figure of bias under the assumption that the posteriors are Gaussian and uncorrelated. We notice that this is a conservative choice, since choosing a metric that takes the correlations into consideration would lead to larger values for the parameter shifts. In addition, we report a fit-quality diagnostic, $\Delta\chi^2_\nu$ defined as the difference between the reduced effective fit statistic of the tested and the baseline models, evaluated at the maximum posterior point of each sample (Krause et al. 2021; Campos et al. 2023). This metric is intended to quantify the relative degradation in goodness-of-fit between the data vector and the model under study. Since our chains store a posterior rather than an explicit likelihood χ^2, we used this quantity as a descriptive diagnostic and did not assign it a formal probability-to-exceed threshold.

We also examine cases in which we kept the data vectors unchanged and only tested the impact of changing the prior width of some parameters. This was quantified in terms of constraining power, which was simply computed as the percent difference between the parameter errors with the baseline prior width and with the different width that we were testing.

Table 1. Reference values and priors on the nuisance parameters we are testing.

Name	Value	Prior type	Prior width or range
Intrinsic alignment parameters			
$\mathcal{A}_{\rm IA}$	0.16	Uniform	$[-2, 2]$
$\eta_{\rm IA}$	1.66	Uniform	$[0, 3]$
Photometric galaxy bias parameters			
$b_{\rm gph,0}$	1.33291	Uniform	$[-3, 3]$
$b_{\rm gph,1}$	−0.72414	Uniform	$[-3, 3]$
$b_{\rm gph,2}$	1.01830	Uniform	$[-3, 3]$
$b_{\rm gph,3}$	−0.14913	Uniform	$[-3, 3]$
Photometric magnification bias parameters			
$b_{\rm mag,0}$	−1.50685	Uniform	$[-3, 3]$
$b_{\rm mag,1}$	1.35034	Uniform	$[-3, 3]$
$b_{\rm mag,2}$	0.08321	Uniform	$[-3, 3]$
$b_{\rm mag,3}$	0.04279	Uniform	$[-3, 3]$
Photometric redshift shift parameters			
Δz_1	−0.025749	Gaussian	0.00257890
Δz_2	0.022716	Gaussian	0.00275258
Δz_3	−0.026032	Gaussian	0.00287484
Δz_4	0.012594	Gaussian	0.00307264
Δz_5	0.019285	Gaussian	0.00323726
Δz_6	0.008326	Gaussian	0.00341852
Δz_7	0.038207	Gaussian	0.00360394
Δz_8	0.002732	Gaussian	0.00371824
Δz_9	0.034066	Gaussian	0.00395192
Δz_{10}	0.049479	Gaussian	0.00418664
Δz_{11}	0.066490	Gaussian	0.00449286
Δz_{12}	0.000815	Gaussian	0.00497880
Δz_{13}	0.049070	Gaussian	0.00584318
Multiplicative bias parameters			
$m_{i\in\{1,13\}}$	0	Gaussian	0.002
Outlier fraction parameters			
$f_{\rm out,1}$	0.195	Gaussian	0.01
$f_{\rm out,2}$	0.204	Gaussian	0.01
$f_{\rm out,3}$	0.306	Gaussian	0.01
$f_{\rm out,4}$	0.121	Gaussian	0.01

Notes. When the prior is uniform, we specify the range; when Gaussian, we specify the width.

5. Results

In this section we present the results of our analysis in terms of constraints on the cosmological parameters. Figures only show parameter contours that display significant changes with respect to the baseline set-up (always in black). Relevant subsets of nuisance parameter constraints are shown in Appendix A.

The common practice to test for robustness of the analysis pipeline is to check that bias due to different choices in the modelling stays within a certain fraction of the statistical uncertainty. In the following, we report all cases in which $\Delta\sigma_\theta > 0.1$, i.e. more than 10% of the statistical uncertainty.

A summary of the shift in the best-fit parameters and change in the constraining power is given in Tables 2 and 3, respectively. All the files containing the samples for each case are available on Zenodo.

Table 2. Parameter shifts under various data and model assumptions.

Intrinsic alignment							
	H_0	Ω_b	Ω_m	n_s	σ_8	S_8	$\Delta\chi^2_\nu$
d: no IA, m: zNLA	6.54	4.66	5.48	5.69	4.82	2.72	4.63
d: zNLA, m: no IA	0.27	0.41	1.35	0.26	0.06	2.29	0.79
↳ (2×2pt)	0.14	0.32	0.68	0.38	0.66	2.11	1.09
↳ (WL)	0.61	2.04	4.23	1.08	4.49	1.00	0.08

Galaxy bias					
	Ω_m	n_s	σ_8	S_8	$\Delta\chi^2_\nu$
d: polynomial, m: const. per-bin	0.25	0.42	1.28	1.53	0.01
d: polynomial, m: interp. per-bin	0.29	0.11	0.56	0.30	5.4×10^{-4}

Multiplicative bias					
	Ω_m	n_s	σ_8	S_8	$\Delta\chi^2_\nu$
d: $m_i = 0.002$, p: $\mathcal{G}(0, 0.002)$	0.37	0.23	0.09	0.72	1.6×10^{-5}
d: $m_i = 0.002$, p: $\mathcal{G}(0, 0.004)$	0.35	0.24	0.08	0.63	-1.0×10^{-6}
d: $m_i = 0.002$, m: no m-bias	0.37	0.24	0.10	0.78	-3.9×10^{-4}

Notes. The values in this table are the parameter shifts $\Delta\sigma_\theta$ defined in Eq. (19) for the models we test compared to the baseline model. For each case, we specify the data (d), the model (m), or the prior (p), where $\mathcal{G}(m, \sigma)$ indicates a Gaussian centred in m with width σ. The last column reports the relative fit-quality diagnostic $\Delta\chi^2_\nu$ of the test model compared to the baseline model, evaluated at the maximum posterior point of each sample. $\Delta\chi^2_\nu$ values close to zero indicate very similar fit quality, while negative values indicate that the tested setup provides a marginally better fit than the baseline according to this diagnostic. We note that we report changes only on the cosmological parameters which are of interest for each model. Unless otherwise stated in parentheses, it is always a 3×2pt analysis.

5.1. Intrinsic alignment

The amplitude of intrinsic alignment $\mathcal{A}_{IA}$ is consistent with 0 for all Stage III weak lensing surveys (Secco et al. 2022; Dalal et al. 2023; Wright et al. 2025). While it is possible that the signal is very small (Fortuna et al. 2021) and that with the reduced statistical errors from Stage IV surveys we will be able to measure it, two scenarios are possible:

1. if the signal is still small compared to the statistical error and we try to model it with a model that is too complex, we could be impacted by prior volume effects and risk biasing the cosmological parameters;

Table 3. Percentage change in the constraining power of the cosmological parameters for different prior choices.

Redshift shifts			
	Ω_m	σ_8	S_8
$\Delta z_i = 2\times10^{-2}(1+z_i)$	−7.32%	−9.81%	−0.53%
Correlated $\Delta z = 0.0036$	−0.09%	−0.05%	+0.26%
Fixed to reference	+11.69%	+17.38%	+3.97%

Purity		
	$\ln(10^{10}A_s)$	$\Omega_c h^2$
Prior width: 5%	−48.52%	−6.68%
Prior width: 10%	−70.23%	−13.87%

Notes. Each value in this table is the percentage difference (+ denotes increase and − decrease) between the model parameter we test against the baseline model. Baselines: prior width $\Delta z = 2\times10^{-3}(1+z_i)$ for the redshift shifts, and 1% prior for the purity parameters.

2. if the signal has a complex dependency on redshift and other galaxy properties and we try to model it with a simplistic model, due to the large amount of parameters that we are varying this mis-modelling could be re-absorbed by other parameters.

To address the first case, we analysed a data vector with zero intrinsic alignment signal using the baseline zNLA model. As can be seen in Fig. 1, all of the cosmological parameters show important shifts from the baseline, ranging from 2.72 σ for S_8 to 6.54 σ for H_0 (see Table 2). In Fig. A.1, we show the constraints on the IA parameters and the redshift shifts: as expected, the amplitude $\mathcal{A}_{IA}$ gets close to 0 and the power-law index η_{IA} becomes unconstrained, resulting in important shifts on the Δz parameters, confirming previous findings in this direction (Fischbacher et al. 2023). Such large shifts can be attributed to prior-volume effects caused by this nested zNLA parameter structure. We show the maximum a posteriori (MAP) value in Fig. 1 and Fig. A.1 as crosses and dotted lines in the 2D and 1D projected posteriors, respectively. Although in this case the MAP is only marginally different from the projected posterior, we cannot conclude that the prior volume effects are not the root cause of the shifts that we observe. In fact, MAP values might still be affected by prior choices (Gómez-Valent 2022; Holm et al. 2023; Herold et al. 2025). We also report a large $\Delta\chi^2_\nu$ of 4.63 translating the mis-modelling effect into the goodness-of-fit degradation.

We addressed the impact of IA mis-modelling by fitting the baseline data vector, which contains a zNLA signal, without modelling IA at all. The results are shown in Fig. 2 for the cosmological parameters and in Fig. A.2 for the nuisance parameters. We can observe a bias greater than 0.3 σ in most of the cosmological parameters, especially on Ω_m, σ_8, and S_8. We can also see that the size of the contours shrinks because of the smaller parameter space. In terms of nuisance parameters, we can again observe shifts in the Δz parameters, albeit smaller than in the previous case. We also report large $\Delta\chi^2_\nu$ (see again Table 2) indicating mismatch between the data vector and the model.

Samuroff et al. (2024) suggest that IA mis-modelling can be more prominently identified when analysing 2×2pt and WL separately, where the latter would be significantly more biased. We test this in our *Euclid*-specific set-up by running a case where we fit the baseline data vector without any IA modelling. We show the results in Figs. 3 and A.3 for the cosmological and nuisance parameters, respectively. We can indeed confirm that, also in our

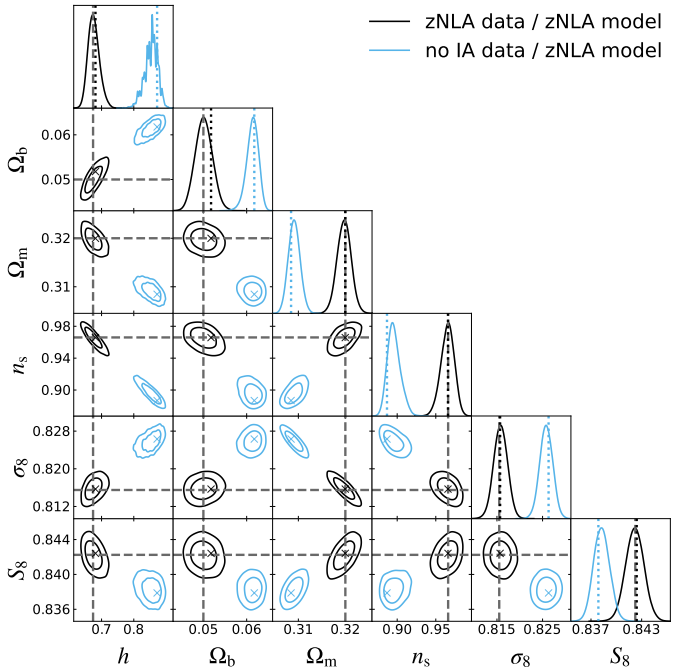

Fig. 1. Cosmological parameter constraints in the baseline case (black), and using the zNLA intrinsic alignment model for a data vector with zero intrinsic alignment signal (blue). The MAP value is shown in the respective colours for the 2D (crosses) and 1D (dotted lines) projected posterior panels. Note: the 1D projected posterior for h looks scattered because the samples are hitting the upper boundary of the prior.

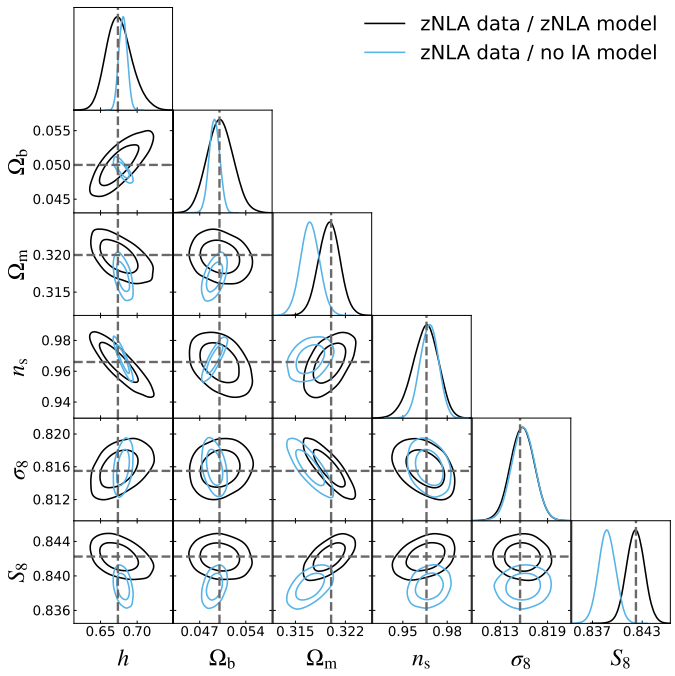

Fig. 2. Cosmological parameter constraints in the baseline case (black), and analysing a data vector with zNLA signal with no intrinsic alignment model (blue).

case, WL is significantly more impacted by IA mis-modelling. In fact, we can observe significant biases in the cosmological and Δz parameters, with a maximum of $4.49\,\sigma$ for σ_8. Similarly, we report large $\Delta\chi^2_\nu$ values confirming the parameter biases.

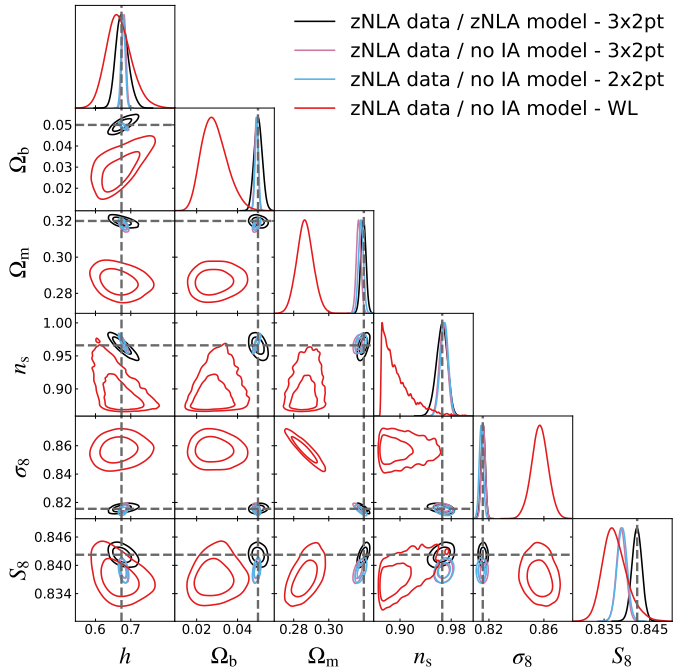

Fig. 3. Cosmological parameter constraints in the baseline case (black), and analysing a data vector with zNLA signal with no intrinsic alignment model using the 3×2 pt combination (purple), 2×2 pt (blue) and WL only (red).

In summary, correctly modelling IA is of the utmost importance in recovering unbiased cosmological parameter constraints from a 3×2pt analysis. Some hints that special care is needed are the presence of poorly constrained nuisance parameters and inconsistencies in the cosmological parameters between the different observables. More in-depth tests of IA mis-modelling have been conducted in Euclid Collaboration: Navarro-Gironés et al. (2026) in the context of the first *Euclid* Data Release. Despite having larger statistical errors, their work also shows that IA mis-modelling can induce significant biases in the cosmological parameters.

5.2. Photometric galaxy bias

In our baseline set-up, we chose a polynomial functional form to describe the redshift evolution of the linear galaxy bias for the photometric sample. While this is a sensible choice, since we expect galaxy bias to evolve smoothly with redshift, a more conservative approach would be to use one galaxy bias parameter per redshift bin. This implies fitting 13 parameters instead of 4, significantly increasing the size of the parameter space and the risk of incurring projection effects.

We tested this by fitting the baseline data vector, generated with a polynomial galaxy bias function, with a model that has a constant value of galaxy bias within each redshift bin. The results are shown in Fig. 4 for cosmological and IA parameters, Fig. A.4 for galaxy bias parameters, and Fig. A.5 for the redshift shift parameters. From these figures, we see that using constant per-bin values (in purple) leads to biases on some of the cosmological parameters, with a maximum of $1.53\,\sigma$ for S_8, and much more important biases on all of the nuisance parameters. We have tested that this does not arise from projection effects alone in the optimistic scale cuts employed in this work by repeating the analysis with a cut at $\ell_{\rm max} = 1500$ for the GCph and

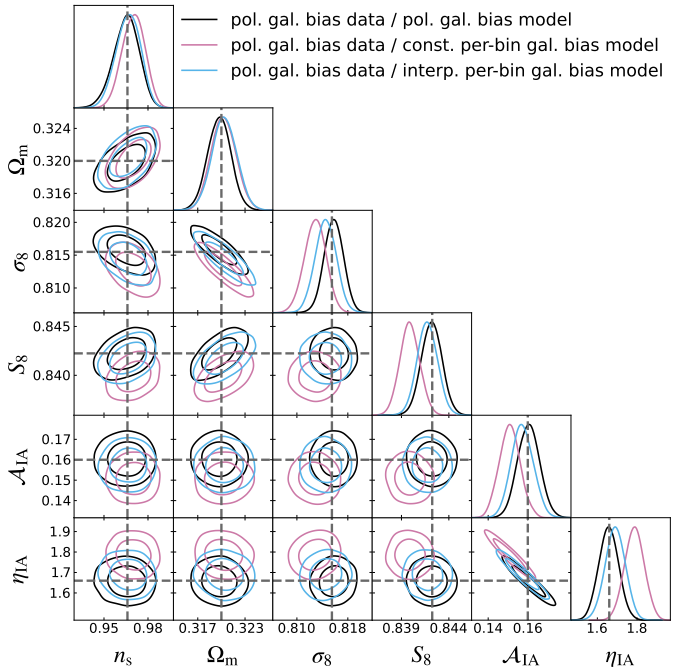

Fig. 4. Constraints on cosmological and IA parameters in the baseline case (black), and analysing the baseline data vector with a constant per-bin galaxy bias model (purple) or with a linear function of redshift within each bin (blue).

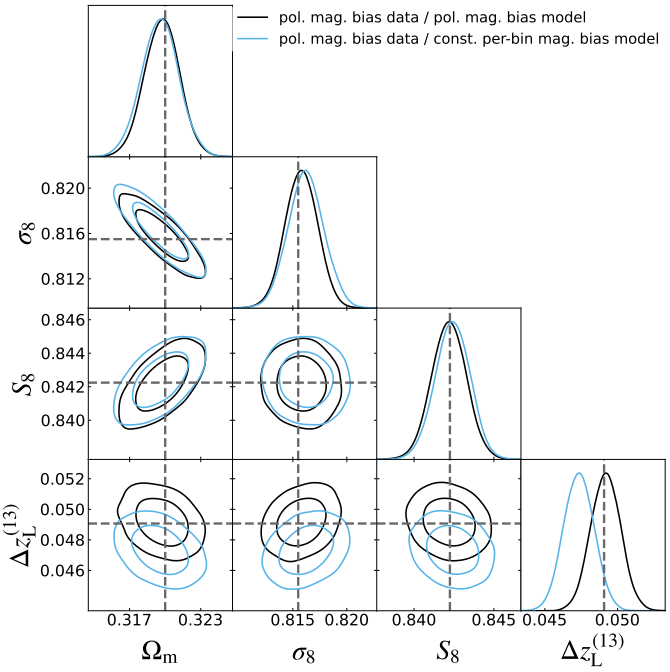

Fig. 5. Parameter constraints in the baseline set-up (black) and when fitting the baseline data vector with a constant per-bin magnification bias model (blue).

XC spectra, which also resulted in a $1.17\,\sigma$ bias on S_8. We also note that in this case the $\Delta\chi^2_\nu$ is low indicating that this metric is not sufficient to capture the bias.

Let us note here that the baseline values for the polynomial galaxy bias parameters have been obtained by fitting the values of galaxy bias at the centre of each redshift bin as measured in the Flagship 2.1 simulation (Euclid Collaboration: Castander et al. 2025). In the simulation, galaxy bias is evolving within the redshift bin, and our measurement is a weighted average over the redshift range of the bin. Assuming that the bias is constant within the bin leads to an unphysical step-like redshift evolution, which can cause most of the differences seen here. We further checked this by fitting the polynomial bias data with the constant per-bin model, but now throwing away the highest redshift bin. This is the widest bin within which there is a lot of redshift evolution that is neglected. We still find a biased constraint (due to the unaccounted-for redshift evolution in the remaining tomographic bins) but somewhat alleviated, finding a shift of $0.98\,\sigma$ for S_8. We thus run an additional case where the galaxy bias is assumed to be a linear function within each redshift bin, which is shown in blue in Figs. 4 and A.5. We note that this model significantly reduces the biases in all of the parameters, with a maximum shift of $0.56\,\sigma$ for σ_8. These tests show that *Euclid* data are rather sensitive to the modelling of the redshift evolution of galaxy bias, highlighting the need for a physically motivated modelling of this systematic effect.

5.3. Magnification bias

Similarly to the case of galaxy bias, our baseline set-up also uses a polynomial function to model the redshift evolution of magnification bias. We tested the impact of using a constant per-bin model to fit our baseline data vector and, as we can see in Fig. 5, in this case we do not observe any bias on the cosmological parameters. However, we can appreciate a $\sim 0.5\,\sigma$ shift on the Δz parameter of the highest redshift bin 13. This is not surprising given the fact that the magnification signal becomes progressively more important at higher redshifts. The contrast of these results with respect to the galaxy bias case can be understood as magnification bias is a subdominant effect compared to galaxy bias, so mis-modelling in the former is less evident than in the latter.

5.4. Shear multiplicative bias

In the ideal case, multiplicative bias can be calibrated, and the m_i parameters can be fixed to zero. In practice, we expect a residual multiplicative bias to remain after calibration. Its magnitude can be estimated and used to set a Gaussian prior on the m_i parameters. Here, we study the impact of the choice of prior on the cosmological parameters.

Note that our baseline prior width is 0.002, which is 4 times larger than the 5×10^{-4} used in Euclid Collaboration: Cañas-Herrera et al. (2025). However, we have checked that the constraints on the cosmological parameters remain indistinguishable. This implies that the size of the prior on the m_i parameters has an insignificant impact on the constraining power.

The first case we examine is the impact of centring the prior at zero when the true value is $1\,\sigma$ away from the centre, where σ here denotes the width of the prior. The results are shown in Fig. 6. We observe a moderate bias of $0.37\,\sigma$ and $0.72\,\sigma$ on Ω_m and S_8, respectively. We then study whether doubling the prior width can resolve this issue, and find very little change, with a bias of $0.35\,\sigma$ and $0.63\,\sigma$ on Ω_m and S_8, respectively. This is almost as bad as not modelling multiplicative bias at all, which is shown in red in Fig. 6. Again, we report low $\Delta\chi^2_\nu$ values and thus biases cannot be detected with this metric alone. These results indicate that care must be taken to ensure that the priors on

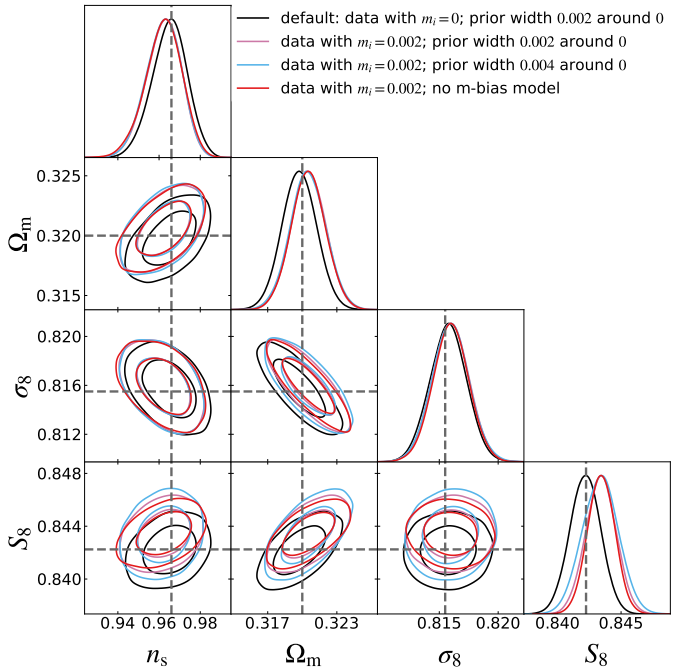

Fig. 6. Cosmological parameter constraints in the baseline case (black), and analysing a data vector with $m_i = 0.002$ with a prior centred at 0 with width 0.002 (purple), with a prior centred at 0 with width 0.004 (blue), and without modelling multiplicative bias (red).

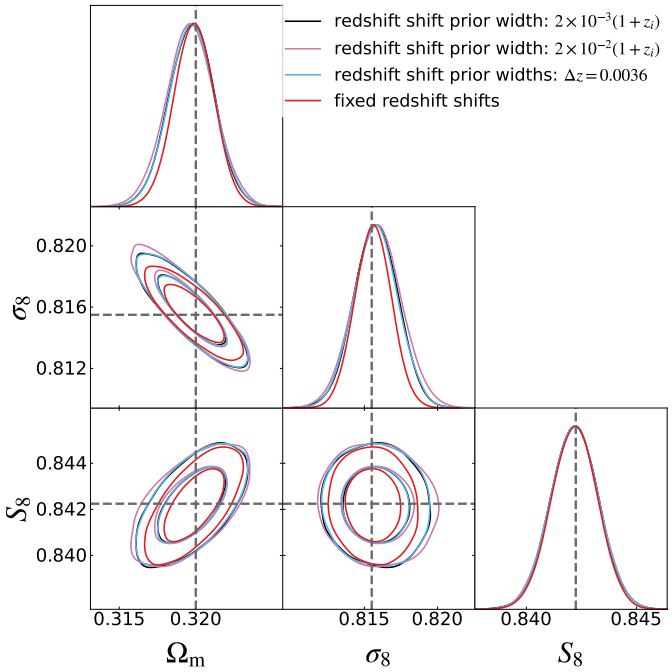

Fig. 7. Cosmological parameter constraints in the baseline case (black), and using a 10 times larger prior (purple), a fully correlated prior with width 0.0036 (blue), and fixing the redshift shifts (red).

multiplicative bias are not too narrow compared to the expected amplitude of the m_i parameters.

5.5. Shift in the mean of the redshift distribution

In our baseline set-up, we modelled the error on the estimation of the redshift distribution by having one nuisance parameter per redshift bin that shifts the mean of the distribution while leaving the shape unchanged. The priors on these shift parameters Δz_i are redshift-dependent and scale as 2×10^{-3} $(1 + z_i)$, where z_i is the centre of the redshift bin (Euclid Collaboration: Mellier et al. 2025).

To check what the impact of the size of the prior on the cosmological parameters is, we ran a case in which the width of the prior is ten times larger. The results are shown in Fig. 7 and Table 3. As expected, we observe a loss of constraining power of 7.32% in Ω_m and 9.81% in σ_8, but their combination S_8 is only marginally affected, with a difference of less than 1%.

Although it is reasonable to expect that the errors in the photometric redshift estimation increase at higher redshift, one could opt for using fully correlated Δz priors with a fixed width for all redshift bins and thus significantly reducing the size of the parameter space to be explored. As can be seen in Fig. 7, this leads to an insignificant change in the contours. This can be understood by looking at Fig. A.6, where we show the size of the posterior compared to the prior. The Δz parameters are well constrained by data, so changes in prior width have minimal impact on the posterior.

We also studied a case in which we fixed all Δz parameters to their reference value, resulting in a gain in constraining power of 11.69% on Ω_m, 17.38% on σ_8, and 3.97% on S_8. This represents the maximum gain that one can achieve by perfectly calibrating the redshift distributions. This is consistent with what was recently shown in Wright et al. (2025) using KiDS Legacy data, where improvements in the calibration of the redshift distributions lead to a 15% gain in constraining power. We refer the reader to Euclid Collaboration: Bertmann et al. (2026) for a more detailed study of the impact of redshift distribution uncertainties in the context of the first *Euclid* Data Release.

5.6. Purity

The size of the prior on the f_{out} parameters reflects our confidence in the estimate of the purity of the sample of Hα galaxies. In our baseline set-up, we assume that we can calibrate the fraction of outliers to within an absolute error of 1%, but this might not be achievable in practice. Therefore, we test the impact of having larger priors on the f_{out} parameters. Results are shown in Figs. 8 and A.7. As expected, the most affected parameter is A_s, which is degenerate with the purity correction in the data vector. Having a 5% (10%) prior width on the outlier fraction parameters decreases the constraining power on A_s by 48.52% (70.23%) and on $\Omega_c h^2$ by 6.68% (13.87%). We also observe a loss in constraining power on the bias and EFT counter-terms parameters, as can be seen in Fig. A.7.

6. Conclusions

In this work, we have studied the impact of modelling and prior choices for the most important systematic effects in the 3×2 pt and spectroscopic galaxy clustering 2pt analyses using synthetic data vectors that mimic the final *Euclid* data release. We have identified several potentially problematic choices that warrant further study.

Among the systematic effects studied here, intrinsic alignment seems to be the most worrisome. For a signal that is expected to be small, using complex models with many parameters can lead to important biases due to prior-volume effects. At the same time, mis-modelling the signal also has an impact on the

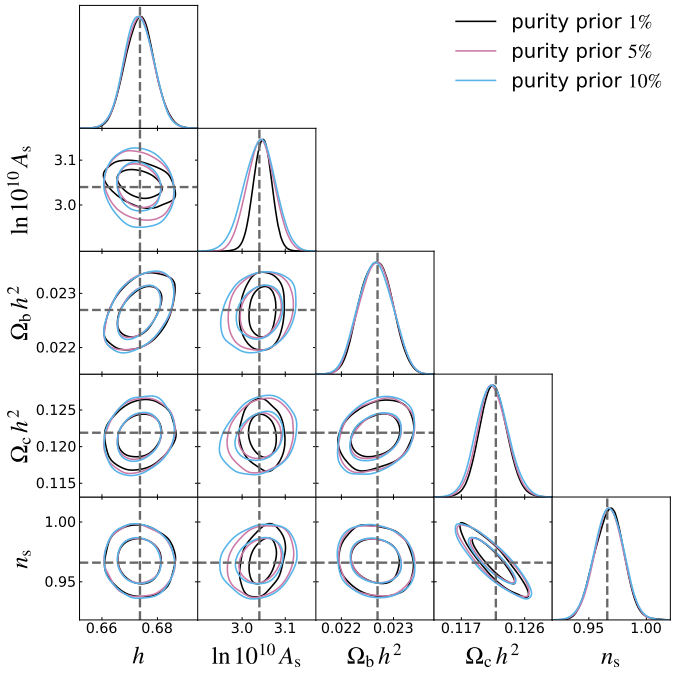

Fig. 8. Cosmological parameter constraints in the baseline case (black), and using a 5% prior (purple) and a 10% prior (blue) on the fraction of outliers.

cosmological parameters, leading to biases of a sizeable fraction of the statistical uncertainty.

From our tests, we can also see that in the final *Euclid* data analysis, we will be somewhat sensitive to the modelling of the redshift evolution of galaxy bias. Even if we assume a reasonable piecewise linear function of redshift, if the true underlying redshift evolution is a more complex function, we could get biases of the order of $0.5\,\sigma$ on some of the cosmological parameters. Along these lines, we should mention that, in this work, we restricted ourselves to tests of linear galaxy models and left the small-scale modelling of the 3×2pt analysis, such as non-linear galaxy bias, various scale cuts, and baryonic effects, to be dealt with in the parallel work of Euclid Collaboration: Carrilho et al. in prep.

For the parameters in which we expect to use Gaussian priors, care must be taken in choosing a width that ensures unbiased constraints while maximising the cosmological information. For instance, we caution against using too optimistic priors on the multiplicative bias parameters, as already having a true value $1\,\sigma$ away from the centre of the prior can induce a considerable bias on the cosmological parameters.

In our set-up, the redshift shifts are well constrained, so that the choice of prior width has little impact on the best-fit parameters. Enlarging the priors does, however, result in a loss of constraining power on the cosmological parameters. Since these parameters seem to be well constrained by the data, it is worth choosing a narrower prior width to gain constraining power.

At the same time, the redshift shift parameters are severely impacted by mis-modelling of other systematic effects. For this reason, it is important that the redshift distributions are well calibrated. Indeed, this has been identified by the community as one of the areas that needs the most improvement. Wright et al. (2025) showed the significant impact of doing so by improving their constraining power by 15% and concurrently resolving the S_8 tension, which seems to have been driven by poorly modelled systematic effects.

On the spectroscopic galaxy clustering side, we have tested the impact of enlarging the prior on the fraction of outliers. As expected, this has a significant impact on the constraining power of A_s, since the two are fully degenerate, but also on $\Omega_c h^2$. From this test, it is clear that a better calibration of the purity can result in significant gains in constraining power from *Euclid* spectroscopic galaxy clustering alone. This work has set the stage for more focused analyses that will consider each of these systematic effects and determine modelling and prior choices for the future *Euclid* data analyses.

7. Data availability

The result samples for all the cases described in our analysis are available on the Zenodo archive https://doi.org/10.5281/zenodo.16029827.

Acknowledgements. KT is supported by the STFC grant ST/W000903/1 and by the European Structural and Investment Fund. The Euclid Consortium acknowledges the European Space Agency and a number of agencies and institutes that have supported the development of *Euclid*, in particular the Agenzia Spaziale Italiana, the Austrian Forschungsförderungsgesellschaft funded through BMIMI, the Belgian Science Policy, the Canadian Euclid Consortium, the Deutsches Zentrum für Luft- und Raumfahrt, the DTU Space and the Niels Bohr Institute in Denmark, the French Centre National d'Etudes Spatiales, the Fundação para a Ciência e a Tecnologia, the Hungarian Academy of Sciences, the Ministerio de Ciencia, Innovación y Universidades, the National Aeronautics and Space Administration, the National Astronomical Observatory of Japan, the Netherlandse Onderzoekschool Voor Astronomie, the Norwegian Space Agency, the Research Council of Finland, the Romanian Space Agency, the Swiss Space Office (SSO) at the State Secretariat for Education, Research, and Innovation (SERI), and the United Kingdom Space Agency. A complete and detailed list is available on the *Euclid* web site (`www.euclid-ec.org/consortium/community/`). The authors acknowledge the contribution of the Lorentz Center (Leiden), and of the European Space Agency (ESA), where the workshop "Making CLOE shine" and the "CLOE workshop 2023" were held. The authors acknowledge the use of the IRIS computing facility in the UK. StC acknowledges support from the Italian Ministry of University and Research (MUR), PRIN 2022 'EXSKALIBUR Euclid-Cross-SKA: Likelihood Inference Building for Universe's Research', Grant No. 20222BBYB9, CUP D53D2300252 0006, and from the European Union – Next Generation EU.

References

Abbott, T., Abdalla, F. B., Allam, S., et al. 2016, PRD, 94, 022001
Abbott, T. M. C., Abdalla, F. B., Annis, J., et al. 2018, MNRAS, 480, 3879
Alam, S., Albareti, F. D., Allende Prieto, C., et al. 2015, ApJS, 219, 12
Alsing, J., Kirk, D., Heavens, A., & Jaffe, A. H. 2015, MNRAS, 452, 1202
Berlfein, F., Mandelbaum, R., Dodelson, S., & Schafer, C. 2024, MNRAS, 531, 4954
Bernstein, G. M. 2010, MNRAS, 406, 2793
Blazek, J., Vlah, Z., & Seljak, U. 2015, JCAP, 8, 015
Campos, A., Samuroff, S., & Mandelbaum, R. 2023, MNRAS, 525, 18851901
Carrilho, P., Moretti, C., & Pourtsidou, A. 2023, JCAP, 1, 028
Cooke, R. J., Pettini, M., & Steidel, C. C. 2018, ApJ, 855, 102
Cragg, C., Duncan, C. A. J., Miller, L., & Alonso, D. 2022, MNRAS, 518, 4909
Cropper, M., Hoekstra, H., Kitching, T., et al. 2013, MNRAS, 431, 3103
Cropper, M., Pottinger, S., Niemi, S., et al. 2016, in Society of Photo-Optical Instrumentation Engineers (SPIE) Conference Series, Vol. 9904, Space Telescopes and Instrumentation 2016: Optical, Infrared, and Millimeter Wave, ed. H. A. MacEwen, G. G. Fazio, M. Lystrup, N. Batalha, N. Siegler, & E. C. Tong, 99040Q
Dalal, R., Li, X., Nicola, A., et al. 2023, PRD, 108, 123519
DES Collaboration: Abbott, T. M. C., Aguena, M., Alarcon, A., et al. 2025, arXiv e-prints, arXiv:2503.13632
Donald-McCann, J., Gsponer, R., Zhao, R., Koyama, K., & Beutler, F. 2023, MNRAS, 526, 3461
Duncan, C. A. J., Joachimi, B., Heavens, A. F., Heymans, C., & Hildebrandt, H. 2013, MNRAS, 437, 2471
Eriksen, M. & Hoekstra, H. 2018, MNRAS, 477, 3433
Euclid Collaboration: Bertmann, K. A., Porredon, A., Duret, V., et al. 2026, A&A, submitted, arXiv:2604.00805
Euclid Collaboration: Cañas-Herrera, G., Goh, L. W. K., Blot, L., et al. 2025, A&A, accepted, arXiv:2510.09153

Euclid Collaboration: Cardone, V. F., Joudaki, S., Blot, L., et al. 2025, A&A, accepted, arXiv:2510.09118
Euclid Collaboration: Castander, F., Fosalba, P., Stadel, J., et al. 2025, A&A, 697, A5
Euclid Collaboration: Congedo, G., Miller, L., Taylor, A. N., et al. 2024, A&A, 691, A319
Euclid Collaboration: Cropper, M., Al-Bahlawan, A., Amiaux, J., et al. 2025, A&A, 697, A2
Euclid Collaboration: Desprez, G., Paltani, S., Coupon, J., et al. 2020, A&A, 644, A31
Euclid Collaboration: Joudaki, S., Pettorino, V., Blot, L., et al. 2026, A&A, accepted, arXiv:2603.22475
Euclid Collaboration: Lepori, F., Tutusaus, I., Viglione, C., et al. 2022, A&A, 662, A93
Euclid Collaboration: Martinelli, M., Pezzotta, A., Sciotti, D., et al. 2025, A&A, accepted, arXiv:2510.09141
Euclid Collaboration: Martinet, N., Schrabback, T., Hoekstra, H., et al. 2019, A&A, 627, A59
Euclid Collaboration: McCracken, H. J., Benson, K., Dolding, C., et al. 2025, A&A, in press (Euclid Q1 SI), https://doi.org/10.1051/0004-6361/202554594, arXiv:2503.15303
Euclid Collaboration: Mellier, Y., Abdurro'uf, Acevedo Barroso, J., et al. 2025, A&A, 697, A1
Euclid Collaboration: Navarro-Gironés, D., Tutusaus, I., Crocce, M., et al. 2026, A&A, submitted, arXiv:2602.16448
Euclid Collaboration: Paykari, P., Kitching, T., Hoekstra, H., et al. 2020, A&A, 635, A139
Euclid Collaboration: Risso, I., Veropalumbo, A., Branchini, E., et al. 2026, A&A, 707, A233
Euclid Collaboration: Schirmer, M., Jahnke, K., Seidel, G., et al. 2022, A&A, 662, A92
Euclid Collaboration: Tanidis, K., Cardone, V. F., Martinelli, M., et al. 2024, A&A, 683, A17
Fischbacher, S., Kacprzak, T., Blazek, J., & Refregier, A. 2023, JCAP, 1, 033
Fortuna, M. C., Hoekstra, H., Joachimi, B., et al. 2021, MNRAS, 501, 2983
Garcia-Quintero, C., Ishak, M., & Ning, O. 2020, JCAP, 12, 018
Gómez-Valent, A. 2022, PRD, 106, 063506
Heavens, A., Alsing, J., & Jaffe, A. H. 2013, MNRAS, 433, L6
Herold, L., Ferreira, E. G. M., & Heinrich, L. 2025, PRD, 111, 083504
Hildebrandt, H., van Waerbeke, L., & Erben, T. 2009, A&A, 507, 683
Hoekstra, H., Viola, M., & Herbonnet, R. 2017, MNRAS, 468, 3295
Holm, E. B., Herold, L., Simon, T., et al. 2023, PRD, 108, 123514
Huterer, D., Takada, M., Bernstein, G., & Jain, B. 2006, MNRAS, 366, 101
Ivanov, M. M., McDonough, E., Hill, J. C., et al. 2020, PRD, 102, 103502
Ivezić, v., Kahn, S. M., Tyson, A. J., et al. 2019, ApJ, 873, 111
Jansen, H., Tewes, M., Schrabback, T., et al. 2024, A&A, 683, A240
Joachimi, B., Cacciato, M., Kitching, T. D., et al. 2015, SSR, 193, 1
Joachimi, B., Mandelbaum, R., Abdalla, F. B., & Bridle, S. L. 2011, A&A, 527, A26
Joudaki, S. & Kaplinghat, M. 2012, PRD, 86, 023526
Kaiser, N. 1987, MNRAS, 227, 1
Kaiser, N. 1992, ApJ, 388, 272
Kannawadi, A., Hoekstra, H., Miller, L., et al. 2019, A&A, 624, A92
Kitching, T. D., Paykari, P., Hoekstra, H., & Cropper, M. 2019, OJAp, 2, 5
Krause, E., Fang, X., Pandey, S., et al. 2021, arXiv e-prints, arXiv:2105.13548
Lange, J. U. 2023, MNRAS, 525, 3181
Li, S.-S., Hoekstra, H., Kuijken, K., et al. 2023, A&A, 679, A133
Liu, J., Ortiz-Vazquez, A., & Hill, J. C. 2016, PRD, 93
LSST Dark Energy Science Collaboration: Awan, H., Gawiser, E., Sanchez, J., & Sevilla-Noarbe, I. 2025, JCAP, 03, 064
LSST Dark Energy Science Collaboration: Mandelbaum, R., Eifler, T., Hložek, R., et al. 2018, arXiv e-prints, arXiv: 1809.01669
LSST Science Collaboration: Abell, P., A., Allison, J., Anderson, S., F., et al. 2009, arXiv e-prints, arXiv:0912.0201
Mandelbaum, R. 2018, ARA&A, 56, 393
Massey, R., Hoekstra, H., Kitching, T., et al. 2013, MNRAS, 429, 661
Maus, M., Chen, S.-F., & White, M. 2023, JCAP, 6, 005
Mead, A. J., Brieden, S., Tröster, T., & Heymans, C. 2021, MNRAS, 502, 1401
Melchior, P. & Viola, M. 2012, MNRAS, 424, 2757
Morawetz, J., Zhang, H., Bonici, M., et al. 2025, arXiv e-prints, arXiv:2508.11811
Myles, J., Alarcon, A., Amon, A., et al. 2021, MNRAS, 505, 4249
Ménard, B., Scranton, R., Fukugita, M., et al. 2010, MNRAS, 405, 1025
Naidoo, K., Johnston, H., Joachimi, B., et al. 2023, A&A, 670, A149
Novell-Masot, S., Gil-Marín, H., Verde, L., et al. 2025, JCAP, 2025, 005
Pujol, A., Sureau, F., Bobin, J., et al. 2020, A&A, 641, A164
Refregier, A., Kacprzak, T., Amara, A., Bridle, S., & Rowe, B. 2012, MNRAS, 425, 1951
Samuroff, S., Campos, A., Porredon, A., & Blazek, J. 2024, OJAp, 7, 40
Schmidt, F., Rozo, E., Dodelson, S., Hui, L., & Sheldon, E. 2009a, ApJ, 702, 593
Schmidt, F., Rozo, E., Dodelson, S., Hui, L., & Sheldon, E. 2009b, PRL, 103, 051301
Schutt, T., Jarvis, M., Roodman, A., et al. 2025, OJAp, 8
Schöneberg, N. 2024, JCAP, 2024, 006
Schöneberg, N., Verde, L., Gil-Marín, H., & Brieden, S. 2022, JCAP, 2022, 039
Scranton, R., Ménard, B., Richards, G. T., et al. 2005, ApJ, 633, 589
Secco, L. F., Samuroff, S., Krause, E., et al. 2022, PRD, 105, 023515
Semboloni, E., Hoekstra, H., Huang, Z., et al. 2013, MNRAS, 432, 2385
Simon, T., Zhang, P., Poulin, V., & Smith, T. L. 2023, PRD, 107, 123530
Sun, L., Fan, Z.-H., Tao, C., et al. 2009, ApJ, 699, 958
Tanidis, K. & Camera, S. 2019, MNRAS, 489, 3385
Tanidis, K., Camera, S., & Parkinson, D. 2019, MNRAS, 491, 4869
Tutusaus, I., Martinelli, M., Cardone, V. F., et al. 2020, A&A, 643, A70
van Uitert, E. & Schneider, P. 2016, A&A, 595, A93
Wright, A. H., Stölzner, B., Asgari, M., et al. 2025, A&A, 703, A158
Zhao, R., Mu, X., Gsponer, R., et al. 2024, MNRAS, 532, 783

[1] Center for Data-Driven Discovery, Kavli IPMU (WPI), UTIAS, The University of Tokyo, Kashiwa, Chiba 277-8583, Japan
[2] Laboratoire d'etude de l'Univers et des phenomenes eXtremes, Observatoire de Paris, Université PSL, Sorbonne Université, CNRS, 92190 Meudon, France
[3] Department of Physics, Oxford University, Keble Road, Oxford OX1 3RH, UK
[4] European Space Agency/ESTEC, Keplerlaan 1, 2201 AZ Noordwijk, The Netherlands
[5] Leiden Observatory, Leiden University, Einsteinweg 55, 2333 CC Leiden, The Netherlands
[6] Department of Physics, Astronomy and Mathematics, University of Hertfordshire, College Lane, Hatfield AL10 9AB, UK
[7] Institute for Astronomy, University of Edinburgh, Royal Observatory, Blackford Hill, Edinburgh EH9 3HJ, UK
[8] Waterloo Centre for Astrophysics, University of Waterloo, Waterloo, Ontario N2L 3G1, Canada
[9] INAF-IASF Milano, Via Alfonso Corti 12, 20133 Milano, Italy
[10] Dipartimento di Fisica, Università degli Studi di Torino, Via P. Giuria 1, 10125 Torino, Italy
[11] INFN-Sezione di Torino, Via P. Giuria 1, 10125 Torino, Italy
[12] INAF-Osservatorio Astrofisico di Torino, Via Osservatorio 20, 10025 Pino Torinese (TO), Italy
[13] INAF-Osservatorio Astronomico di Roma, Via Frascati 33, 00078 Monteporzio Catone, Italy
[14] INFN-Sezione di Roma, Piazzale Aldo Moro, 2 - c/o Dipartimento di Fisica, Edificio G. Marconi, 00185 Roma, Italy
[15] Institute for Theoretical Particle Physics and Cosmology (TTK), RWTH Aachen University, 52056 Aachen, Germany
[16] Deutsches Zentrum für Luft- und Raumfahrt e. V. (DLR), Linder Höhe, 51147 Köln, Germany
[17] INFN-Sezione di Genova, Via Dodecaneso 33, 16146, Genova, Italy
[18] Dipartimento di Fisica, Università di Genova, Via Dodecaneso 33, 16146, Genova, Italy
[19] Université Paris-Saclay, Université Paris Cité, CEA, CNRS, AIM, 91191, Gif-sur-Yvette, France
[20] Institut d'Estudis Espacials de Catalunya (IEEC), Edifici RDIT, Campus UPC, 08860 Castelldefels, Barcelona, Spain
[21] Institute of Space Sciences (ICE, CSIC), Campus UAB, Carrer de Can Magrans, s/n, 08193 Barcelona, Spain
[22] Université Paris-Saclay, CNRS/IN2P3, IJCLab, 91405 Orsay, France
[23] Institut de Recherche en Astrophysique et Planétologie (IRAP), Université de Toulouse, CNRS, UPS, CNES, 14 Av. Edouard Belin, 31400 Toulouse, France
[24] Centro de Investigaciones Energéticas, Medioambientales y Tecnológicas (CIEMAT), Avenida Complutense 40, 28040 Madrid, Spain
[25] INAF-Osservatorio Astronomico di Trieste, Via G. B. Tiepolo 11, 34143 Trieste, Italy
[26] IFPU, Institute for Fundamental Physics of the Universe, via Beirut 2, 34151 Trieste, Italy
[27] INFN, Sezione di Trieste, Via Valerio 2, 34127 Trieste TS, Italy

[28] SISSA, International School for Advanced Studies, Via Bonomea 265, 34136 Trieste TS, Italy
[29] INAF-Osservatorio Astronomico di Brera, Via Brera 28, 20122 Milano, Italy
[30] Institut für Theoretische Physik, University of Heidelberg, Philosophenweg 16, 69120 Heidelberg, Germany
[31] Université St Joseph; Faculty of Sciences, Beirut, Lebanon
[32] Max Planck Institute for Extraterrestrial Physics, Giessenbachstr. 1, 85748 Garching, Germany
[33] LINKS Foundation, Via Pier Carlo Boggio, 61 10138 Torino, Italy
[34] Institute for Particle Physics and Astrophysics, Dept. of Physics, ETH Zurich, Wolfgang-Pauli-Strasse 27, 8093 Zurich, Switzerland
[35] INAF-Osservatorio di Astrofisica e Scienza dello Spazio di Bologna, Via Piero Gobetti 93/3, 40129 Bologna, Italy
[36] INFN-Sezione di Bologna, Viale Berti Pichat 6/2, 40127 Bologna, Italy
[37] DAMTP, Centre for Mathematical Sciences, Wilberforce Road, Cambridge CB3 0WA, UK
[38] Kavli Institute for Cosmology Cambridge, Madingley Road, Cambridge, CB3 0HA, UK
[39] Institut d'Astrophysique de Paris, UMR 7095, CNRS, and Sorbonne Université, 98 bis boulevard Arago, 75014 Paris, France
[40] Dipartimento di Fisica e Scienze della Terra, Università degli Studi di Ferrara, Via Giuseppe Saragat 1, 44122 Ferrara, Italy
[41] Istituto Nazionale di Fisica Nucleare, Sezione di Ferrara, Via Giuseppe Saragat 1, 44122 Ferrara, Italy
[42] Dipartimento di Fisica e Astronomia "Augusto Righi" - Alma Mater Studiorum Università di Bologna, via Piero Gobetti 93/2, 40129 Bologna, Italy
[43] Université de Genève, Département de Physique Théorique and Centre for Astroparticle Physics, 24 quai Ernest-Ansermet, CH-1211 Genève 4, Switzerland
[44] Instituto de Física de Cantabria, Edificio Juan Jordá, Avenida de los Castros, 39005 Santander, Spain
[45] Higgs Centre for Theoretical Physics, School of Physics and Astronomy, The University of Edinburgh, Edinburgh EH9 3FD, UK
[46] Aix-Marseille Université, Université de Toulon, CNRS, CPT, Marseille, France
[47] Departamento de Física, FCFM, Universidad de Chile, Blanco Encalada 2008, Santiago, Chile
[48] Mathematical Institute, University of Leiden, Einsteinweg 55, 2333 CA Leiden, The Netherlands
[49] Center for Cosmology and AstroParticle Physics, The Ohio State University, 191 West Woodruff Avenue, Columbus, OH 43210, USA
[50] Department of Physics, The Ohio State University, Columbus, OH 43210, USA
[51] Dipartimento di Fisica e Astronomia, Università di Bologna, Via Gobetti 93/2, 40129 Bologna, Italy
[52] Department of Physics "E. Pancini", University Federico II, Via Cinthia 6, 80126, Napoli, Italy
[53] INAF-Osservatorio Astronomico di Capodimonte, Via Moiariello 16, 80131 Napoli, Italy
[54] Port d'Informació Científica, Campus UAB, C. Albareda s/n, 08193 Bellaterra (Barcelona), Spain
[55] INFN section of Naples, Via Cinthia 6, 80126, Napoli, Italy
[56] Institute for Astronomy, University of Hawaii, 2680 Woodlawn Drive, Honolulu, HI 96822, USA
[57] Dipartimento di Fisica e Astronomia "Augusto Righi" - Alma Mater Studiorum Università di Bologna, Viale Berti Pichat 6/2, 40127 Bologna, Italy
[58] Instituto de Astrofísica de Canarias, Vía Láctea, 38205 La Laguna, Tenerife, Spain
[59] Jodrell Bank Centre for Astrophysics, Department of Physics and Astronomy, University of Manchester, Oxford Road, Manchester M13 9PL, UK
[60] European Space Agency/ESRIN, Largo Galileo Galilei 1, 00044 Frascati, Roma, Italy
[61] ESAC/ESA, Camino Bajo del Castillo, s/n., Urb. Villafranca del Castillo, 28692 Villanueva de la Cañada, Madrid, Spain
[62] Université Claude Bernard Lyon 1, CNRS/IN2P3, IP2I Lyon, UMR 5822, Villeurbanne, F-69100, France
[63] Institut de Ciències del Cosmos (ICCUB), Universitat de Barcelona (IEEC-UB), Martí i Franquès 1, 08028 Barcelona, Spain
[64] Institució Catalana de Recerca i Estudis Avançats (ICREA), Passeig de Lluís Companys 23, 08010 Barcelona, Spain
[65] Institut de Ciencies de l'Espai (IEEC-CSIC), Campus UAB, Carrer de Can Magrans, s/n Cerdanyola del Vallés, 08193 Barcelona, Spain
[66] UCB Lyon 1, CNRS/IN2P3, IUF, IP2I Lyon, 4 rue Enrico Fermi, 69622 Villeurbanne, France
[67] Mullard Space Science Laboratory, University College London, Holmbury St Mary, Dorking, Surrey RH5 6NT, UK
[68] Departamento de Física, Faculdade de Ciências, Universidade de Lisboa, Edifício C8, Campo Grande, PT1749-016 Lisboa, Portugal
[69] Instituto de Astrofísica e Ciências do Espaço, Faculdade de Ciências, Universidade de Lisboa, Campo Grande, 1749-016 Lisboa, Portugal
[70] Department of Astronomy, University of Geneva, ch. d'Ecogia 16, 1290 Versoix, Switzerland
[71] Aix-Marseille Université, CNRS, CNES, LAM, Marseille, France
[72] Université Paris-Saclay, CNRS, Institut d'astrophysique spatiale, 91405, Orsay, France
[73] INFN-Padova, Via Marzolo 8, 35131 Padova, Italy
[74] Aix-Marseille Université, CNRS/IN2P3, CPPM, Marseille, France
[75] INAF-Istituto di Astrofisica e Planetologia Spaziali, via del Fosso del Cavaliere, 100, 00100 Roma, Italy
[76] Space Science Data Center, Italian Space Agency, via del Politecnico snc, 00133 Roma, Italy
[77] INFN-Bologna, Via Irnerio 46, 40126 Bologna, Italy
[78] University Observatory, LMU Faculty of Physics, Scheinerstrasse 1, 81679 Munich, Germany
[79] INAF-Osservatorio Astronomico di Padova, Via dell'Osservatorio 5, 35122 Padova, Italy
[80] Universitäts-Sternwarte München, Fakultät für Physik, Ludwig-Maximilians-Universität München, Scheinerstrasse 1, 81679 München, Germany
[81] Institute of Theoretical Astrophysics, University of Oslo, P.O. Box 1029 Blindern, 0315 Oslo, Norway
[82] Jet Propulsion Laboratory, California Institute of Technology, 4800 Oak Grove Drive, Pasadena, CA, 91109, USA
[83] Department of Physics, Lancaster University, Lancaster, LA1 4YB, UK
[84] Felix Hormuth Engineering, Goethestr. 17, 69181 Leimen, Germany
[85] Technical University of Denmark, Elektrovej 327, 2800 Kgs. Lyngby, Denmark
[86] Cosmic Dawn Center (DAWN), Denmark
[87] Max-Planck-Institut für Astronomie, Königstuhl 17, 69117 Heidelberg, Germany
[88] NASA Goddard Space Flight Center, Greenbelt, MD 20771, USA
[89] Department of Physics and Astronomy, University College London, Gower Street, London WC1E 6BT, UK
[90] Department of Physics and Helsinki Institute of Physics, Gustaf Hällströmin katu 2, University of Helsinki, 00014 Helsinki, Finland
[91] Department of Physics, P.O. Box 64, University of Helsinki, 00014 Helsinki, Finland
[92] Helsinki Institute of Physics, Gustaf Hällströmin katu 2, University of Helsinki, 00014 Helsinki, Finland
[93] SKAO, Jodrell Bank, Lower Withington, Macclesfield SK11 9FT, UK
[94] Centre de Calcul de l'IN2P3/CNRS, 21 avenue Pierre de Coubertin 69627 Villeurbanne Cedex, France
[95] Dipartimento di Fisica "Aldo Pontremoli", Università degli Studi di Milano, Via Celoria 16, 20133 Milano, Italy
[96] INFN-Sezione di Milano, Via Celoria 16, 20133 Milano, Italy
[97] Universität Bonn, Argelander-Institut für Astronomie, Auf dem Hügel 71, 53121 Bonn, Germany
[98] Department of Physics, Institute for Computational Cosmology, Durham University, South Road, Durham, DH1 3LE, UK

[99] Université Paris Cité, CNRS, Astroparticule et Cosmologie, 75013 Paris, France
[100] CNRS-UCB International Research Laboratory, Centre Pierre Binétruy, IRL2007, CPB-IN2P3, Berkeley, USA
[101] Institut d'Astrophysique de Paris, 98bis Boulevard Arago, 75014, Paris, France
[102] Institute of Physics, Laboratory of Astrophysics, Ecole Polytechnique Fédérale de Lausanne (EPFL), Observatoire de Sauverny, 1290 Versoix, Switzerland
[103] Telespazio UK S.L. for European Space Agency (ESA), Camino bajo del Castillo, s/n, Urbanizacion Villafranca del Castillo, Villanueva de la Cañada, 28692 Madrid, Spain
[104] Institut de Física d'Altes Energies (IFAE), The Barcelona Institute of Science and Technology, Campus UAB, 08193 Bellaterra (Barcelona), Spain
[105] DARK, Niels Bohr Institute, University of Copenhagen, Jagtvej 155, 2200 Copenhagen, Denmark
[106] Department of Physics and Astronomy, University of Waterloo, Waterloo, Ontario N2L 3G1, Canada
[107] Perimeter Institute for Theoretical Physics, Waterloo, Ontario N2L 2Y5, Canada
[108] Centre National d'Etudes Spatiales – Centre spatial de Toulouse, 18 avenue Edouard Belin, 31401 Toulouse Cedex 9, France
[109] Institute of Space Science, Str. Atomistilor, nr. 409 Măgurele, Ilfov, 077125, Romania
[110] Dipartimento di Fisica e Astronomia "G. Galilei", Università di Padova, Via Marzolo 8, 35131 Padova, Italy
[111] Universität Innsbruck, Institut für Astro- und Teilchenphysik, Technikerstr. 25/8, 6020 Innsbruck, Austria
[112] Satlantis, University Science Park, Sede Bld 48940, Leioa-Bilbao, Spain
[113] Department of Physics, Royal Holloway, University of London, Surrey TW20 0EX, UK
[114] Instituto de Astrofísica e Ciências do Espaço, Faculdade de Ciências, Universidade de Lisboa, Tapada da Ajuda, 1349-018 Lisboa, Portugal
[115] Cosmic Dawn Center (DAWN)
[116] Niels Bohr Institute, University of Copenhagen, Jagtvej 128, 2200 Copenhagen, Denmark
[117] Universidad Politécnica de Cartagena, Departamento de Electrónica y Tecnología de Computadoras, Plaza del Hospital 1, 30202 Cartagena, Spain
[118] Kapteyn Astronomical Institute, University of Groningen, PO Box 800, 9700 AV Groningen, The Netherlands
[119] Infrared Processing and Analysis Center, California Institute of Technology, Pasadena, CA 91125, USA
[120] INAF, Istituto di Radioastronomia, Via Piero Gobetti 101, 40129 Bologna, Italy
[121] Astronomical Observatory of the Autonomous Region of the Aosta Valley (OAVdA), Loc. Lignan 39, I-11020, Nus (Aosta Valley), Italy
[122] Université Côte d'Azur, Observatoire de la Côte d'Azur, CNRS, Laboratoire Lagrange, Bd de l'Observatoire, CS 34229, 06304 Nice cedex 4, France
[123] Instituto de Física Teórica UAM-CSIC, Campus de Cantoblanco, 28049 Madrid, Spain
[124] Dipartimento di Fisica, Sapienza Università di Roma, Piazzale Aldo Moro 2, 00185 Roma, Italy
[125] Aurora Technology for European Space Agency (ESA), Camino bajo del Castillo, s/n, Urbanizacion Villafranca del Castillo, Villanueva de la Cañada, 28692 Madrid, Spain
[126] Zentrum für Astronomie, Universität Heidelberg, Philosophenweg 12, 69120 Heidelberg, Germany
[127] ICL, Junia, Université Catholique de Lille, LITL, 59000 Lille, France
[128] ICSC - Centro Nazionale di Ricerca in High Performance Computing, Big Data e Quantum Computing, Via Magnanelli 2, Bologna, Italy
[129] CERCA/ISO, Department of Physics, Case Western Reserve University, 10900 Euclid Avenue, Cleveland, OH 44106, USA
[130] Technical University of Munich, TUM School of Natural Sciences, Physics Department, James-Franck-Str. 1, 85748 Garching, Germany
[131] Max-Planck-Institut für Astrophysik, Karl-Schwarzschild-Str. 1, 85748 Garching, Germany
[132] Laboratoire Univers et Théorie, Observatoire de Paris, Université PSL, Université Paris Cité, CNRS, 92190 Meudon, France
[133] Departamento de Física Fundamental. Universidad de Salamanca. Plaza de la Merced s/n. 37008 Salamanca, Spain
[134] IRFU, CEA, Université Paris-Saclay 91191 Gif-sur-Yvette Cedex, France
[135] Université de Strasbourg, CNRS, Observatoire astronomique de Strasbourg, UMR 7550, 67000 Strasbourg, France
[136] Dipartimento di Fisica - Sezione di Astronomia, Università di Trieste, Via Tiepolo 11, 34131 Trieste, Italy
[137] California Institute of Technology, 1200 E California Blvd, Pasadena, CA 91125, USA
[138] Departamento Física Aplicada, Universidad Politécnica de Cartagena, Campus Muralla del Mar, 30202 Cartagena, Murcia, Spain
[139] INFN, Sezione di Lecce, Via per Arnesano, CP-193, 73100, Lecce, Italy
[140] Department of Mathematics and Physics E. De Giorgi, University of Salento, Via per Arnesano, CP-I93, 73100, Lecce, Italy
[141] INAF-Sezione di Lecce, c/o Dipartimento Matematica e Fisica, Via per Arnesano, 73100, Lecce, Italy
[142] CEA Saclay, DFR/IRFU, Service d'Astrophysique, Bat. 709, 91191 Gif-sur-Yvette, France
[143] Institute of Cosmology and Gravitation, University of Portsmouth, Portsmouth PO1 3FX, UK
[144] Department of Computer Science, Aalto University, PO Box 15400, Espoo, FI-00 076, Finland
[145] Instituto de Astrofísica de Canarias, c/ Via Lactea s/n, La Laguna 38200, Spain. Departamento de Astrofísica de la Universidad de La Laguna, Avda. Francisco Sanchez, La Laguna, 38200, Spain
[146] Ruhr University Bochum, Faculty of Physics and Astronomy, Astronomical Institute (AIRUB), German Centre for Cosmological Lensing (GCCL), 44780 Bochum, Germany
[147] Department of Physics and Astronomy, Vesilinnantie 5, University of Turku, 20014 Turku, Finland
[148] Serco for European Space Agency (ESA), Camino bajo del Castillo, s/n, Urbanizacion Villafranca del Castillo, Villanueva de la Cañada, 28692 Madrid, Spain
[149] ARC Centre of Excellence for Dark Matter Particle Physics, Melbourne, Australia
[150] Centre for Astrophysics & Supercomputing, Swinburne University of Technology, Hawthorn, Victoria 3122, Australia
[151] Department of Physics and Astronomy, University of the Western Cape, Bellville, Cape Town, 7535, South Africa
[152] Department of Astrophysics, University of Zurich, Winterthurerstrasse 190, 8057 Zurich, Switzerland
[153] Department of Physics, Centre for Extragalactic Astronomy, Durham University, South Road, Durham, DH1 3LE, UK
[154] Univ. Grenoble Alpes, CNRS, Grenoble INP, LPSC-IN2P3, 53, Avenue des Martyrs, 38000, Grenoble, France
[155] INAF-Osservatorio Astrofisico di Arcetri, Largo E. Fermi 5, 50125, Firenze, Italy
[156] Centro de Astrofísica da Universidade do Porto, Rua das Estrelas, 4150-762 Porto, Portugal
[157] Instituto de Astrofísica e Ciências do Espaço, Universidade do Porto, CAUP, Rua das Estrelas, PT4150-762 Porto, Portugal
[158] Dipartimento di Fisica, Università di Roma Tor Vergata, Via della Ricerca Scientifica 1, Roma, Italy
[159] INFN, Sezione di Roma 2, Via della Ricerca Scientifica 1, Roma, Italy
[160] HE Space for European Space Agency (ESA), Camino bajo del Castillo, s/n, Urbanizacion Villafranca del Castillo, Villanueva de la Cañada, 28692 Madrid, Spain
[161] INAF - Osservatorio Astronomico d'Abruzzo, Via Maggini, 64100, Teramo, Italy

[162] Theoretical astrophysics, Department of Physics and Astronomy, Uppsala University, Box 516, 751 37 Uppsala, Sweden
[163] Institute of Astronomy, University of Cambridge, Madingley Road, Cambridge CB3 0HA, UK
[164] Univ. Lille, CNRS, Centrale Lille, UMR 9189 CRIStAL, 59000 Lille, France
[165] Department of Astrophysical Sciences, Peyton Hall, Princeton University, Princeton, NJ 08544, USA
[166] Space physics and astronomy research unit, University of Oulu, Pentti Kaiteran katu 1, FI-90014 Oulu, Finland
[167] Institut de Physique Théorique, CEA, CNRS, Université Paris-Saclay 91191 Gif-sur-Yvette Cedex, France
[168] Center for Computational Astrophysics, Flatiron Institute, 162 5th Avenue, 10010, New York, NY, USA
[169] International Centre for Theoretical Physics (ICTP), Strada Costiera 11, 34151 Trieste, Italy

Appendix A: Nuisance parameter constraints

In this appendix, we show the parameter constraints of the relevant nuisance parameters for the different cases explored in Sect. 5.

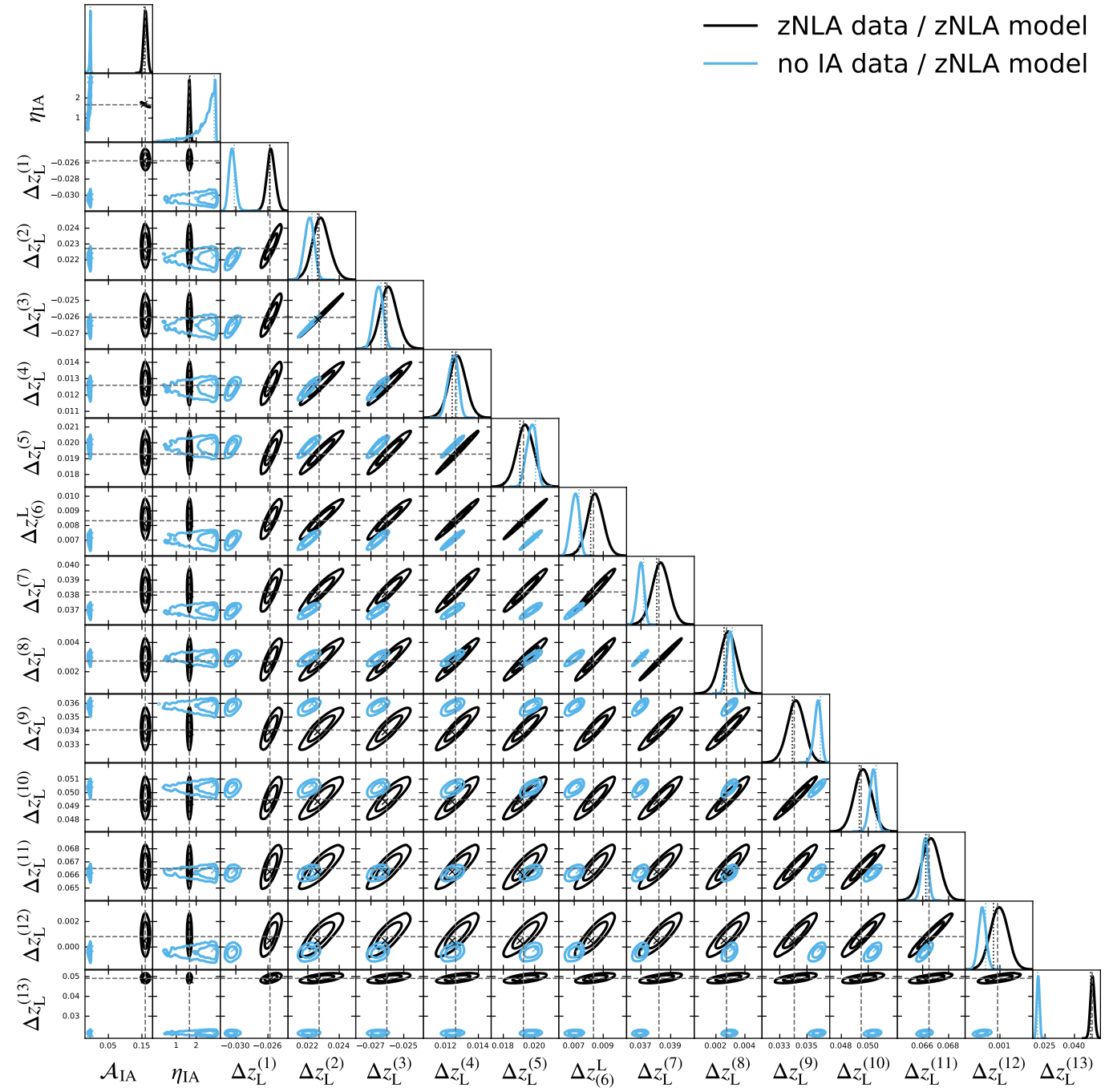

Fig. A.1. Nuisance parameter constraints in the baseline case (black), and using the zNLA intrinsic alignment model for a data vector with zero intrinsic alignment signal (blue). The MAP value is shown in the respective colours for the 2D (crosses) and 1D (dotted lines) projected posterior panels.

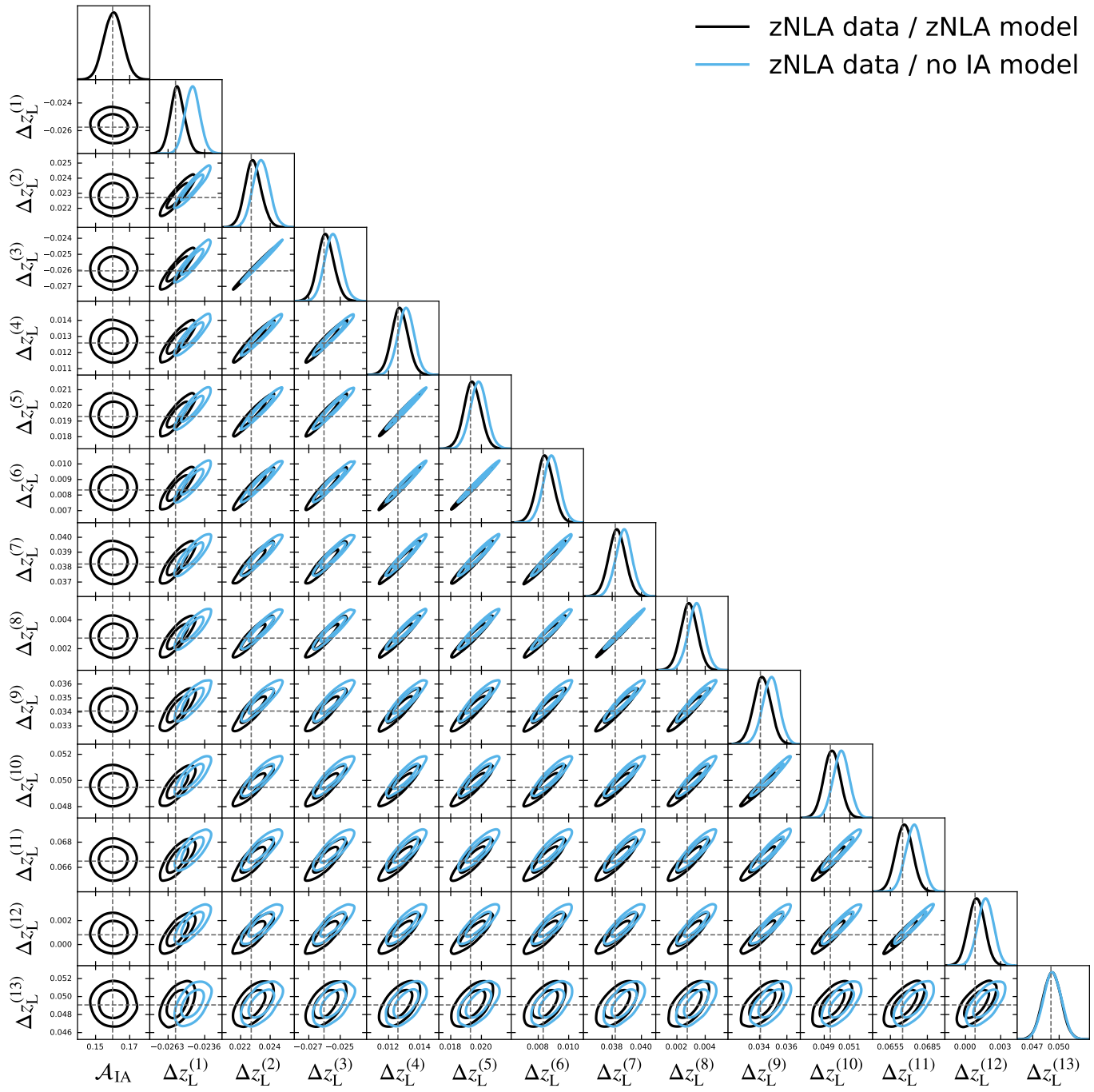

Fig. A.2. Nuisance parameter constraints in the baseline case (black), and analysing a data vector with zNLA signal with no intrinsic alignment model (blue).

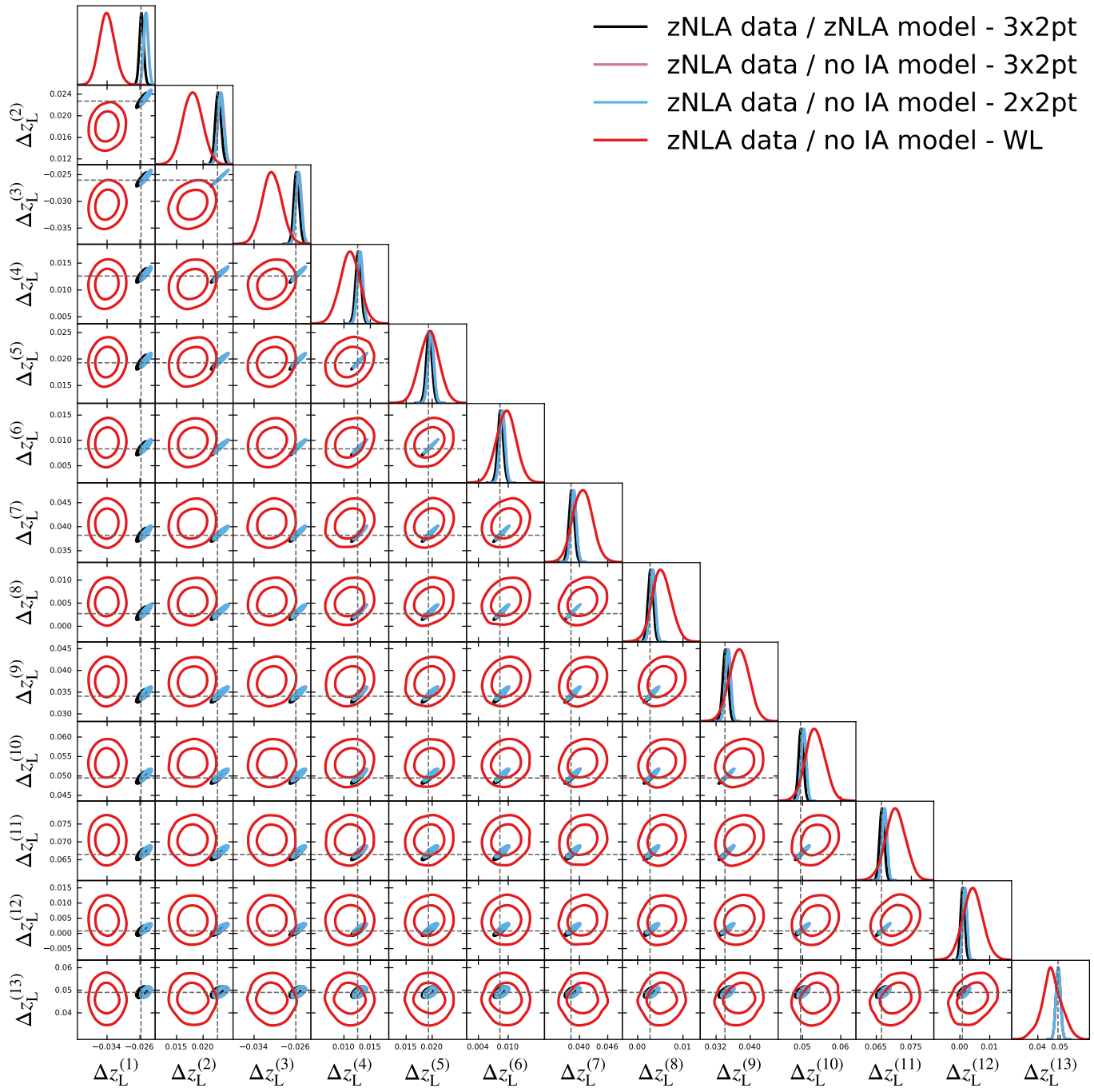

Fig. A.3. Nuisance parameter constraints in the baseline case (black), and analysing a data vector with zNLA signal with no intrinsic alignment model using the 3×2 pt combination (purple), 2×2 pt (blue) and WL only (red). Note: The purple and blue contours are overlapping due to the large range of the axes, but do not coincide.

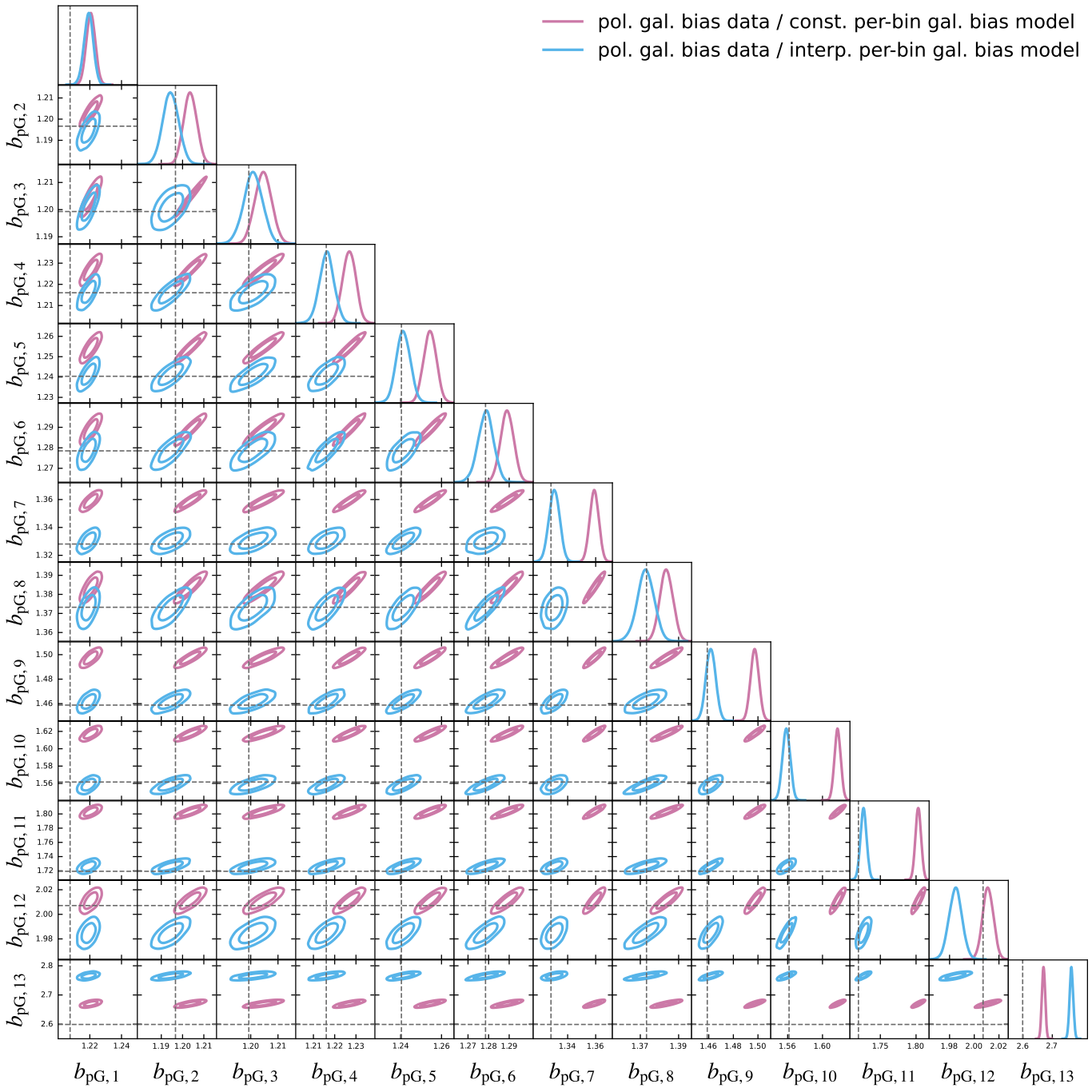

Fig. A.4. Constraints on the per-bin galaxy bias parameters when analysing the baseline data vector with a constant per-bin galaxy bias model (purple) or with a linear function of redshift within each bin (blue).

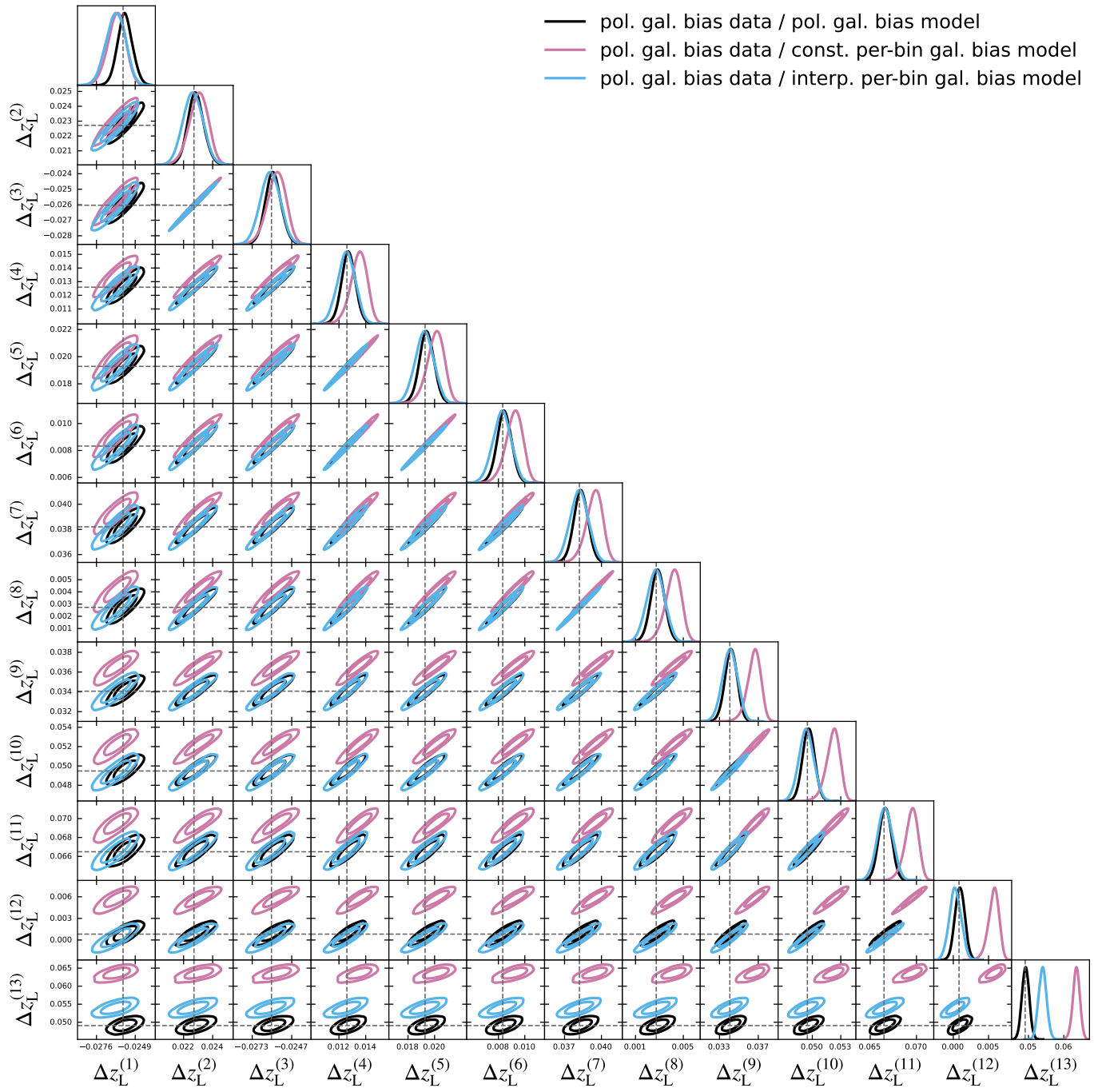

Fig. A.5. Constraints on the redshift shift parameters in the baseline case (black), and analysing the baseline data vector with a constant per-bin galaxy bias model (purple) or with a linear function of redshift within each bin (blue).

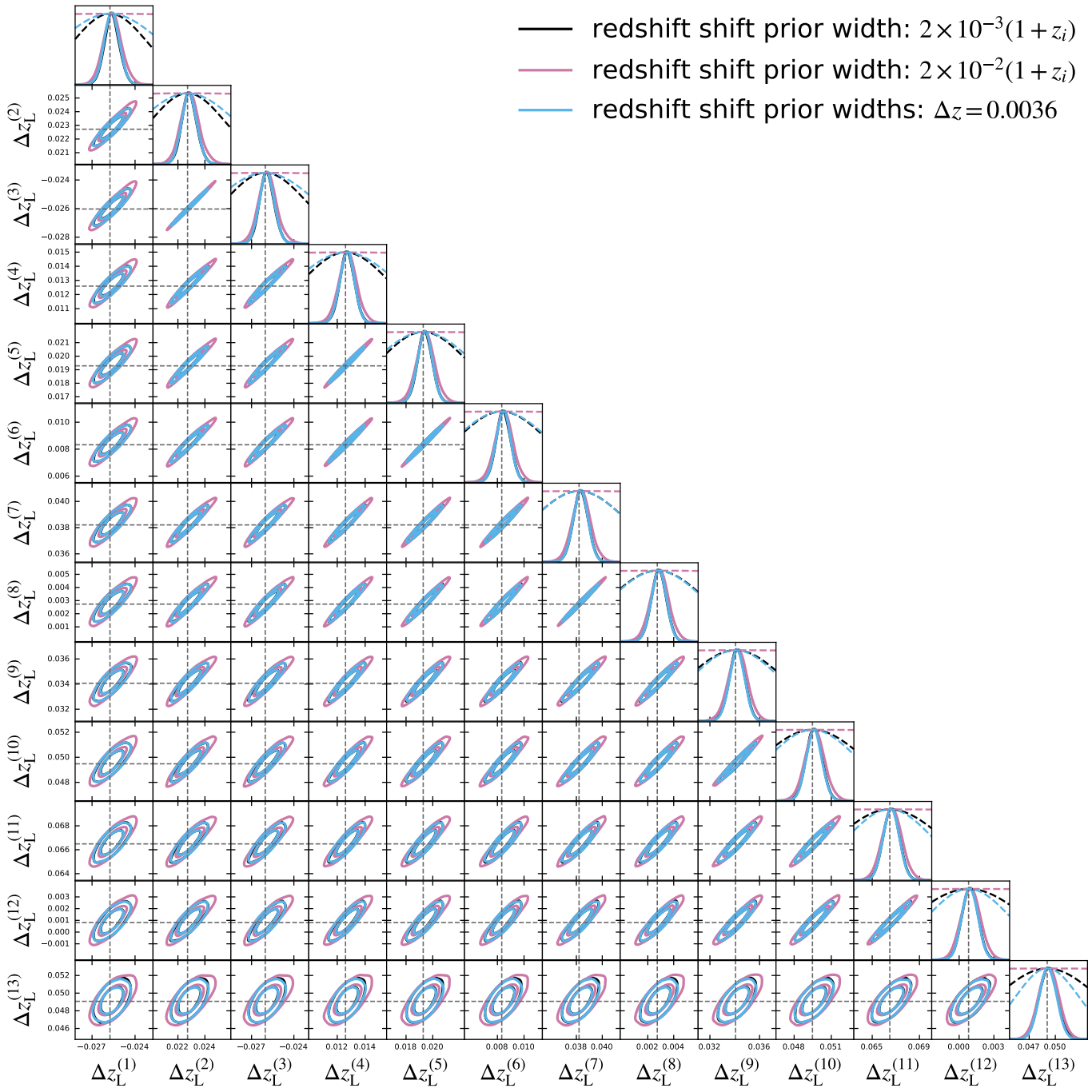

Fig. A.6. Redshift shift parameter constraints in the baseline case (black), and using a 10 times larger prior (purple) and a fully correlated prior with width 0.0036 (blue). Dashed lines show the prior distribution.

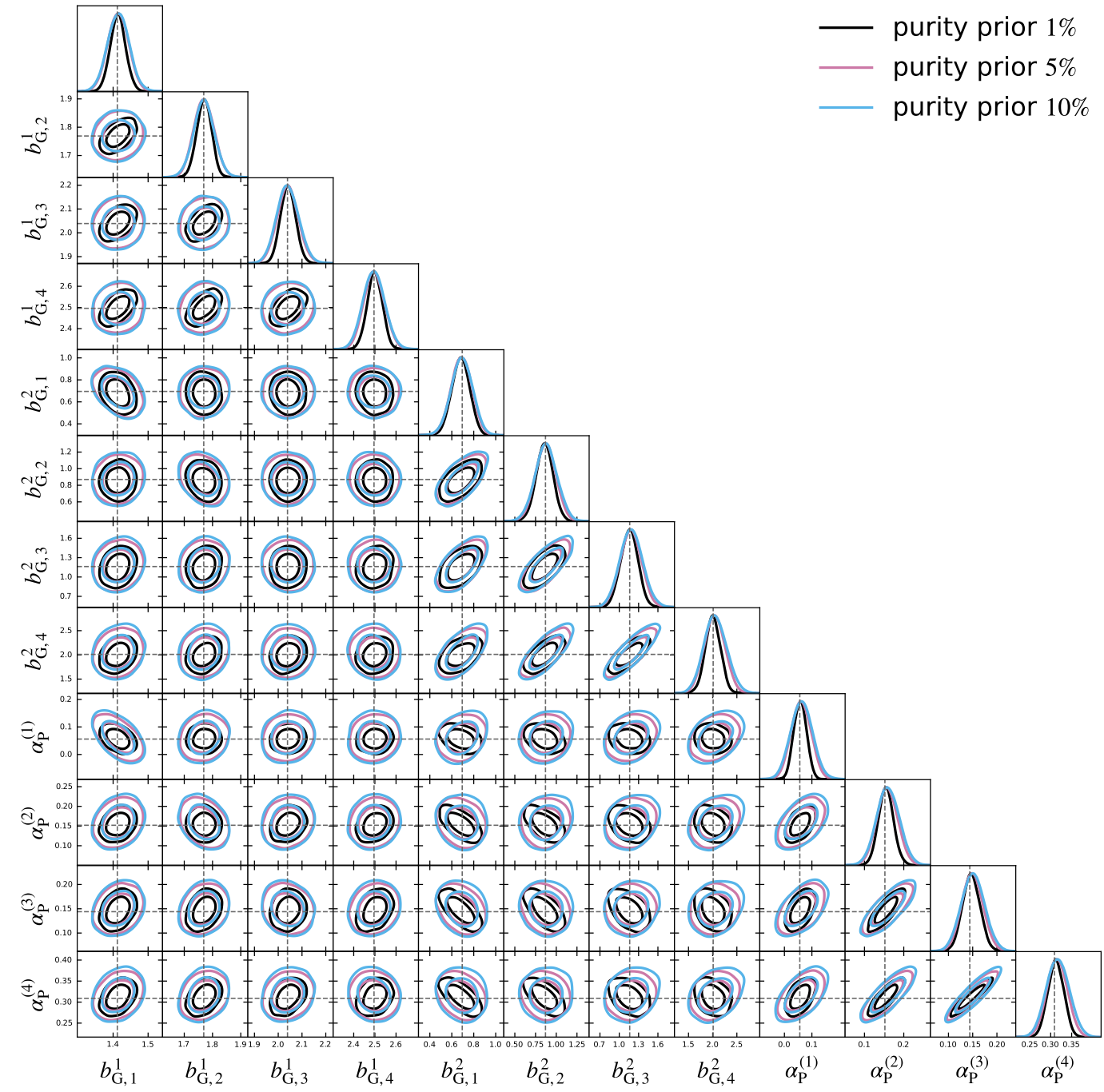

Fig. A.7. EFT nuisance parameter constraints in the baseline case (black), and using a 5 times larger prior (purple) and a 10 times larger prior (blue) on the fraction of outliers.

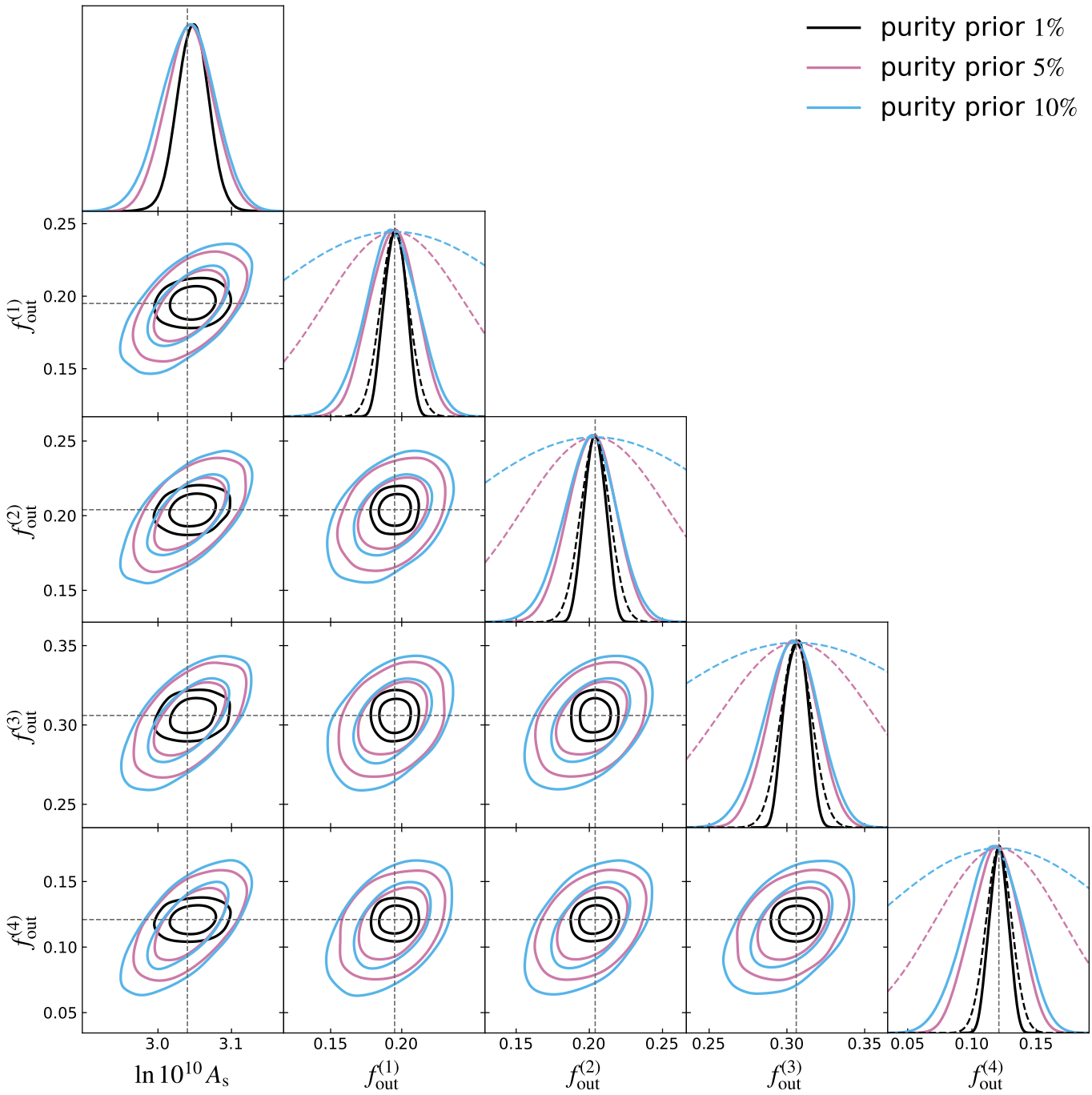

Fig. A.8. f_{out} parameter constraints versus $\ln(10^{10}A_s)$ in the baseline case (black), and using a 5% prior (purple) and a 10% prior (blue) on the fraction of outliers. Dashed lines show the prior distribution.